The Meteoritical Society

Meteoritics & Planetary Science 42, Nr 9, 1473–1493 (2007)
Abstract available online at http://meteoritics.org

Tsunami generation and propagation from the Mjølnir asteroid impact

S. GLIMSDAL[1, 6, 7*], G. K. PEDERSEN[3, 6], H. P. LANGTANGEN[1, 2], V. SHUVALOV[5], and H. DYPVIK[4]

[1]Simula Research Laboratory, Lysaker, Norway
[2]Department of Informatics, University of Oslo, Oslo, Norway
[3]Department of Mathematics, Mechanics Division, University of Oslo, Oslo, Norway
[4]Department of Geosciences, University of Oslo, Oslo, Norway
[5]Institute for Dynamics of Geospheres, Russian Academy of Sciences, Moscow, Russia
[6]International Centre for Geohazards, Oslo, Norway
[7]Norwegian Geotechnical Institute, Oslo, Norway
[*]Corresponding author. E-mail: sgl@ngi.no

(Received 20 March 2006; revision accepted 12 January 2007)

Abstract–In the late Jurassic period, about 142 million years ago, an asteroid hit the shallow paleo-Barents Sea, north of present-day Norway. The geological structure resulting from the impact is today known as the Mjølnir crater. The present work attempts to model the generation and the propagation of the tsunami from the Mjølnir impact. A multi-material hydrocode SOVA is used to model the impact and the early stages of tsunami generation, while models based on shallow-water theories are used to study the subsequent wave propagation in the paleo-Barents Sea. We apply several wave models of varying computational complexity. This includes both three-dimensional and radially symmetric weakly dispersive and nonlinear Boussinesq equations, as well as equations based on nonlinear ray theory. These tsunami models require a reconstruction of the bathymetry of the paleo-Barents Sea.

The Mjølnir tsunami is characteristic of large bolides impacting in shallow sea; in this case the asteroid was about 1.6 km in diameter and the water depth was around 400 m. Contrary to earthquake- and slide-generated tsunamis, this tsunami featured crucial dispersive and nonlinear effects: a few minutes after the impact, the ocean surface was formed into an undular bore, which developed further into a train of solitary waves. Our simulations indicate wave amplitudes above 200 m, and during shoaling the waves break far from the coastlines in rather deep water. The tsunami induced strong bottom currents, in the range of 30–90 km/h, which presumably caused a strong reworking of bottom sediments with dramatic consequences for the marine environment.

INTRODUCTION

Our understanding of impacts by asteroids and comets and their related processes has developed dramatically during the last few decades. Over the last few years in particular, attention has focused on the consequences of marine impacts, and specifically on the development of tsunamis (e.g., see Bourgeois et al. 1988; Gisler et al. 2003; Shuvalov et al. 2002; Smit et al. 1996). The present paper attempts to contribute to this knowledge base by studying the tsunami generated from a specific marine impact of a fairly large object on a shallow continental shelf.

Of the approximately 174 impact craters on Earth currently known (Gersonde et al. 2002; Grieve et al. 1995), 26 have been recognized as original marine impacts (Dypvik et al. 2003, 2004a). Considering that two-thirds of the Earth's surface is covered by water, the number of known terrestrial impacts suggests that many more craters should be found in the oceanic environment. The reduced marine-crater representation is due to several reasons. First, due to plate tectonics, no deep ocean floor older than 200 million years is preserved, while on land very old Precambrian crust is present in large areas. Second, we have limited knowledge of fine-scale topography and structural characteristics of the oceans, and lack constraints on the morphology expected for impact structures formed in the thin oceanic crust. Moreover, impacts in deep ocean are less likely to cause craters because bolides break down when passing through the water column and before in the sea floor impact. The latter point is demonstrated by the Eltanin event (Gersonde et al. 2002; Kyte et al. 1981)

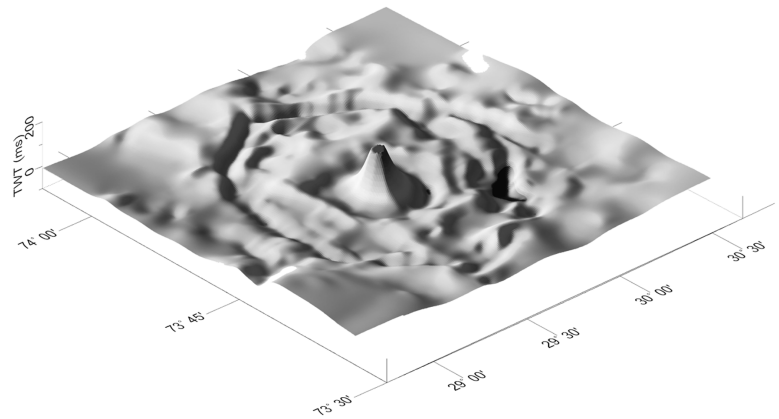

Fig. 1. A seismic reconstruction of the Mjølnir crater (Dypvik et al. 1996).

(2.2 million years ago). In this case, a bolide presumably 1 km in diameter hit the 5000 m deep waters of the South Pacific Ocean. While ejecta and chemical signatures are evident, no crater has been found.

The circular Mjølnir structure was first identified in a seismic survey motivated by the search for oil in the Barents Sea (Gudlaugsson 1993). Subsequent investigations, including corings inside and close to the structure, confirmed the structure to be an impact crater (Dypvik et al. 1996; Smelror et al. 2001; Tsikalas et al. 1998). In addition to breccia, shocked quartz, and an excess of iridium, the core samples revealed a bloom of the green algae *Leiosphaerida* in the sediment layers from the time of impact. Paleontological analysis dates the impact to the late Jurassic, 142 ± 2.6 million years ago. Simulations assuming an asteroid with a diameter of 1.6 km and impact velocity of 20 km/s show that the water was initially blown away (Shuvalov et al. 2002). A tsunami was formed, and the water did not return permanently to the impact site until 15–20 min after the impact. A crater 40 km in diameter was formed on the sea floor (Fig. 1), and vaporized asteroid and target rocks along with crushed material were ejected. Occurrences of large amounts of soot particles in the sediments (Wolbach et al. 2001) show that the organic-rich sediments of the sea floor were ignited when the sea-floor was exposed to the atmosphere. (Dypvik et al., Forthcoming).

After impact, the crater was subsequently reshaped and modified by mass flows, avalanches, and resurge of water into the crater (Dypvik et al. 2004b; Tsikalas 2004). The currents and waves (tsunami) generated by the impact may have significantly affected the sedimentation in the region (Dypvik et al. 2004b). Some sediment reworking has been registered within the Mjølnir crater (Dypvik et al. 2004b) and in a core sample from drill hole 7430 (Fig. 2) adjacent to the crater (Dypvik et al. 1996). Probably hundreds of years passed before the region returned to depositional conditions comparable to the pre-impact state (Dypvik et al. 2004b; Shuvalov et al. 2002). Tsunami influence, and erosional effects in particular, would be expected along the sandier coastlines of the paleo-Barents Sea at that time. Possible indications of these effects are found in shallow cores from the Barents Sea (Dypvik et al., Forthcoming).

For impact-generated tsunamis, both nonlinearity and dispersion remain important for a long time after generation. This is different from most tsunamis originating from other sources. Submarine earthquakes and mass flows generally produce waves with amplitudes of only a few meters. Such tsunamis are linear during generation as well as propagation, while nonlinear effects become significant only close to the shore. Tsunamis of yet other origins, such as airborne slides, huge rock falls, or exploding/collapsing volcanoes, may locally display features reminiscent of impact tsunamis, but the far-field propagation is again linear. Oceanic impacts of asteroids and comets, however, may produce huge waves in the mid-ocean that stay strongly nonlinear during propagation over hundreds and thousands of kilometers.

Impact tsunamis may be categorized into two extreme types. First, small asteroids with diameters much less than the water depth will produce a surface cavity in the sea with elevations at the rim (Artemieva et al. 2002; Gault et al. 1982). The waves evolving from this kind of source will inherit much energy on wavelengths that are short compared to the depth, and are thus highly dispersive. For the Eltanin impact, the disintegration of the impactor, wave generation, and the early phase of tsunami propagation were modeled by Shuvalov (2003). During impact, the ocean surface suffered a violent vertical excursion of several kilometers, while the amplitude of the tsunami's height was on the order of 1 km at a distance of 20 km from the impact center. Gisler et al. (2004) studied tsunami generation by impactors of varying compositions and size (ranging from 250 to 1 km) into water depths of 5000 m. In the impact region interpretations of huge surface excursions as wave height are doubtful; splash-up may be a better term. Still, at a distance of 20 km from the impact center the tsunami amplitudes were well defined and above 1 km for the most energetic bolides. Even though the initial phases of tsunami propagation are strongly affected by

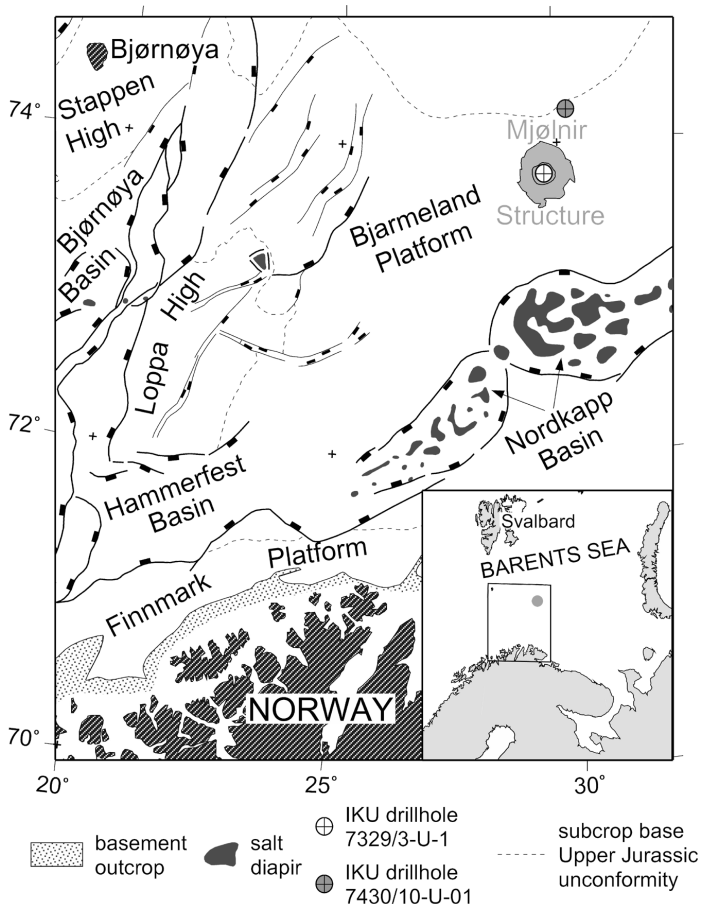

Fig. 2. Current position of the Mjølnir crater in the Barents Sea with major geological lineaments marked.

nonlinearity, dispersion combined with radial spreading will rapidly reduce the amplitudes. Hence, Ward et al. (2000, 2002) employ Fourier transforms combined with optical approximations to describe the far-field tsunami propagation. Korycansky et al. (2005) have studied breaking of typical waves generated by deep-sea impactors with a diameter of less than 1 km. Due to high amplitudes, the waves will break several kilometers offshore on the continental shelf/margin. The breaking of such waves is often called the "Van Dorn effect." Van Dorn et al. (1968) suggested breaking of waves generated by submarine explosions in deep sea, far offshore.

The second extreme class includes large objects that lead to crater formation on the sea floor and a temporarily dry sea bed (Crawford et al. 1998; Gisler et al. 2003; Weiss et al. 2006). In this case the tsunami generation is characterized by intense wave breaking and resurge into the crater. Given that the crater radius is large compared to the water depth, long waves with large amplitudes are eventually formed. Subsequently, these waves will behave very differently from both seismic tsunamis and waves from deep-water impacts. Huge tsunamis of this kind crossing the oceans may lead to strong mixing and sediment transport that may change the environment with drastic consequences for marine life.

In the following, we extend the referenced work on the Mjølnir impact by combining the impact model (Shuvalov et al. 2002) with a dispersive long wave model for tsunami propagation. Since a comparatively fine grid is needed everywhere in the ocean domain, even the long wave model yields heavy computations. Therefore, a simpler strategy based on nonlinear physical optics is adopted and proved to be a valuable tool under the circumstances.

PHYSICAL AND MATHEMATICAL FORMULATION

In the present study, we will focus on the evolution of the tsunamis within a distance of a few thousand kilometers from the impact center. Hence, we may neglect the rotational effects and the curvature of the earth and introduce a Cartesian coordinate system with horizontal axes ox and oy at the undisturbed sea surface. The origin is located at the center of impact. The equilibrium depth is denoted by h and the surface elevation by η. Even for oblique impacts, the later stages of the crater formation and the tsunami generation are nearly symmetric processes (Gisler et al. 2004; Shuvalov et al. 2004). Moreover, the pre-impact bathymetry in the target region probably had a low profile. Therefore, we may

regard the early stages of wave evolution as approximately symmetric and introduce the radii from the impact center, $r = \sqrt{x^2 + y^2}$, as a space variable.

The Impact Model

The impact, cratering, and early stages of tsunami formation were simulated by the SOVA multi-material code (Shuvalov et al. 1999, 2002). This code solves the mass balance equation, the momentum equation, and an energy equation with respect to the total velocity, thermal energy, density, and pressure in a finite volume setting. At each time step, these basic quantities, along with the grid, are advanced using Lagrangian formulations of the governing equations. The solutions are thereafter mapped back to a regular grid. The mapping is constructed in a manner allowing mass, momentum, and energy conservation. The code hence appears as Eulerian, but applies Lagrangian features to locally follow the motion during each time step. When solving two- or three-dimensional equations, SOVA introduces an operator splitting in space that only locally one-dimensional problems are solved implicitly.

The SOVA model includes solid rock, atmospheric air, and water. In addition, passive tracers are introduced to follow trajectories of ejected material. Viscous effects are neglected in the water and air, while the solid rock is modeled as a Bingham fluid with a yield stress expression involving parameters for cohesion, dry friction, limiting material strength, etc. These parameters vary with depth and are tuned so that simulations match the established geological knowledge about the lithology at the time of the impact. The material properties of the sea floor have a large effect on the crater morphology, but only a minor effect on the tsunami generation. At impact the water is blown away, giving rise to a first system of outgoing waves that will be independent of the later stages of the crater formation. On the other hand, the secondary wave systems, created by the resurge of water into the crater, may be influenced by the crater shape. In fact, a huge impact in shallow water may even produce a crater rim that can block the resurge entirely.

Tsunami Propagation Models

During propagation of surface gravity waves, the fluid flow may often be regarded as nonrotational, except in thin boundary layers at the bottom and at the free surface. This is naturally not the case for the region close to the impact where wave breaking and ejecta give rise to a substantial vorticity in the water. However, the vorticity is advected by the particle velocity only and is rapidly left behind the outgoing waves. On the other hand, long-time wave propagation will be affected by the Coriolis force that will induce vertical vorticity. In mid-range, the assumption of nonrotational flow holds and potential theory can be employed.

Oceanic propagation of tsunamis is most frequently described by shallow water theory that neglects deviations from a hydrostatic pressure distribution and yields nondispersive waves. As will be seen subsequently, this theory is completely inadequate for the Mjølnir impact, which generated high and moderately long waves that were genuinely influenced by both nonlinearity and dispersion. The desirable option for such a case is a model based on either the primitive Navier-Stokes equations or full potential theory. However, while we will employ such techniques for the impact itself and the first stages of propagation from the source region, we must resort to a simplified theory for propagation on a larger scale. Our choice is a set of Boussinesq equations that is described in the Appendix.

The coupling between the impact model and the tsunami propagation model is crucial and special care is taken to avoid spurious behavior, such as reflection and noise production. Details are given in Appendix 2.

Optical Approximation and Asymptotic Behavior in the Far-Field

Simulation of the Mjølnir tsunami requires wave models with dispersive effects, such as the Boussinesq equations. These types of models are currently too heavy for simulations of the whole Barents Sea with appropriate resolution. An alternative is to resort to simpler descriptions, such as geometrical and physical optics. Besides significantly increased computational efficiency, the optical theories also provide simple closed-form solutions that render the physics in the wave propagation more transparent. In the present study, we have extensively applied optical methods with success.

When waves of a particular class are propagating in a slowly varying medium, they may adjust gently without loss of identity or noticeable diffraction. This is the basic idea of the optical theories, which are widely used for sinusoidal waves (Mei 1989; Peregrine 1976). Optical descriptions may be employed also for solitary waves (Miles 1977; Reutov 1976; Pedersen 1994). The key point is the identification of the energy density and celerity of the wave as functions of the amplitude and depth. These functions are assumed to be constant in depth, but differ depending on which hydrodynamic theory the optics is based on (full potential theory, Boussinesq theory, asymptotic theory for small amplitudes). Details are given in Appendix 3.

It is instructive to compare the outcome of the simplest version of optics for solitary waves (Equation 21, see Appendix 3) to the counterparts for linear waves. For simplicity, we limit the comparison to cases of radial symmetry. For solitary waves, radial spreading yields an amplitude attenuation $\sim r^{-2/3}$. Correspondingly, linear nondispersive waves, as obtained from the shallow water equations, have an amplitude variation $\sim r^{-1/2}$. Naturally,

every wave will be affected by dispersion, given a sufficient propagation distance. However, in some cases, even the crossing of an ocean will not give dispersive effects time to develop. Tsunamis from impacts, on the other hand, are generally dispersive. Dispersive waves display a diversity of asymptotic behavior with stronger damping rates, as described in, for instance, Mei (1989) and Clarisse et al. (1995). For linear, highly dispersive, and nearly periodic waves, the amplitudes are reduced markedly faster in proportion to r^{-1}. This is the combination of two factors of $r^{-1/2}$ from dispersion and extension of wave crests lengths, respectively. If the motion starts from rest with a net integrated elevation or depression, there is a front of the wave train that attenuates as $r^{-5/6}$, which is also faster than the solitary waves. Different starting conditions may give fronts that attenuate much faster. An initial velocity distribution, with no surface deformation, yields an r^{-1} reduction of the leading wave (Clarisse 1995). However, for an initial elevation that is asymmetric with respect to a line causes an $r^{-4/3}$ damping of the front (Mei 1989). In this case, the trailing waves will eventually dominate, since they still have a damping exponent equal to −1. Numerical computations of impact and wave generation (Gisler et al. 2004) (see Introduction) infer damping rates that are systematically stronger than r^{-1}, with $r^{-2.25}$ up to 100 km from the impact site as the most extreme. However, these are the results of extremely complex computations, where it is difficult to assess all relevant particulars. In general, such damping rates can be explained by breaking, high numerical damping, and under-resolution. They can also be the result of possible misinterpretation of splash-up, wave group dynamics, or interference with compression waves in the water as damping. In shoaling water the amplitude of the solitary wave increases as h^{-1} until breaking, while linear long waves amplify as $h^{-1/4}$. In short, the solitary waves attenuate slower than dispersive deep-water waves and amplify substantially faster than linear waves in shoaling water. We emphasize that the h^{-1} amplification requires very gentle bottom gradients. As will be demonstrated subsequently, it does apply to the bottom slopes of the paleo-Barents Sea. On the other hand, sufficiently mild slopes are not frequent in laboratory experiments, but some experimental support and adequate discussion can be found in Synolakis and Skjelbreia (1993).

THE IMPACT SIMULATION

The impact is simulated with the SOVA code. We have assumed a constant sea depth of 400 m and a normal impact of a 1.6 km asteroid with a velocity of 20 km/s (Shuvalov et al. 2002). However, according to Shuvalov et al. (2004) there is evidence that the Mjølnir impact was oblique, but the crater formation (and hence the generation of the tsunami) is not much affected by an oblique impact. Therefore, we base our work on a normal impact because this allows the application of radially symmetric equations, reducing the number of mathematical dimensions by one, which is highly desirable from a computational point of view.

The grid for the early impact stages is reconstructed several times as the computational domain increases. By reconstruction, we mean a coupling of two neighboring cells into one cell and adding new cells to increase the computational grid. The initial grid has 300 × 500 cells in vertical and horizontal directions, respectively, with an initial cell size of 20 m in both directions. The reconstruction was produced when disturbances induced by the impact reached a boundary of the computational grid. At the late stage, only horizontal cell size was increased (horizontal reconstruction only) because the vertical size of the region of interest (a little bit larger than sea depth) remained constant. In the last phase of the simulations, the resolution decreased to 40 and 160 m in vertical and horizontal directions, respectively.

The results up to 150 s after the impact are shown in Fig. 3. The water was blown away and did not return permanently until after 15–20 min. As previously mentioned, the exposed sea bottom was ignited during this period (Dypvik et al., Forthcoming; Wolbach et al. 2001). After 3 s, the cavity was deeper than 5 km and the radius almost 5 km, while after 30 s the radius of the crater was more than 10 km. Then the short-lived transient crater started to collapse due to the gravitational force, and the central part of the crater rose forming the central height.

In Table 1 we have compared energies from the Mjølnir event to those of the giant earthquake off Sumatra on December 26, 2004. We observe that the total energy in the impact was a factor of 600–700 higher than that of the earthquake. Moreover, integration of the wave energy in the Mjølnir tsunami shows a total of $2.1 \cdot 10^{18}$ J, which is nearly identical to the total energy of the Boxing Day earthquake. The energy of the tsunami from this earthquake is again a factor of 1000 less than that of the Mjølnir tsunami. Naturally, the parameters behind the comparisons are uncertain. Still, it is clear that both the geological consequences and the tsunami of an impact of a large asteroid are orders of magnitude larger than those of even the largest earthquakes recorded.

THE TSUNAMI SIMULATIONS

Modeling of the tsunami from the early stages to the far fields is a complicated task and different type of models and mathematical descriptions must be applied. The very first stages of the tsunami propagation are done by using the SOVA code. The other models are based on long wave theory and are listed in Table 2.

Near-Field Tsunami Evolution

Different early stages of tsunami propagation, as predicted by the SOVA model, are shown in Fig. 4. After

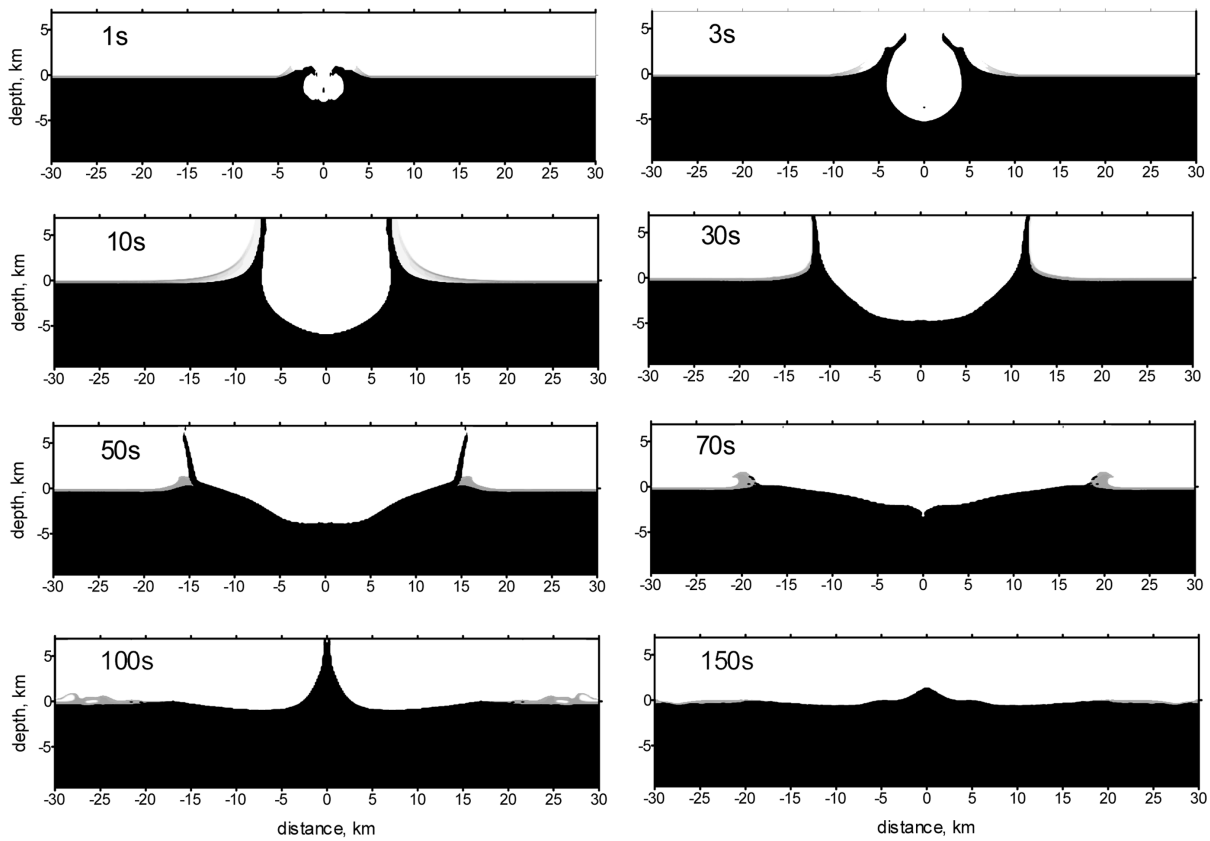

Fig. 3. Impact simulation by SOVA at time steps between 1 and 150 s after impact. The areas colored black indicate sediments and solid rock, while the gray layer above it represents water. The figure is taken from Shuvalov et al. (2002).

Table 1. Energies of the Mjølnir event compared to the Sumatra earthquake, the resulting tsunami in the Indian Ocean, and the Krakatau tsunami in 1883. We have employed a density of 3 kg/dm^3, a diameter of 1.6 km, and a speed of 20 km/s for the Mjølnir impactor. The energy for the December 26, 2004, earthquake is taken from the U.S. Geological Survey home page (USGS 2006). For the Indian Ocean tsunami we assume an initial sea surface elevation of 2 m, over a region of 1200 × 200 km, which yield a high estimate. The energy of the Krakatau tsunami corresponds to an initial cavity of 50 km^2 × 200 m.

Event	Energy
Kinetic energy of the Mjølnir bolide	$1.3 \cdot 10^{22}$ J
Earthquake, December 26, 2004	$2.0 \cdot 10^{18}$ J
Mjølnir tsunami	$2.1 \cdot 10^{18}$ J
Tsunami, December 26, 2004	$3.5 \cdot 10^{15}$ J
Tsunami, Krakatau 1883	$9.6 \cdot 10^{15}$ J

300 s, the vicinity of the central peak is still dry and water is resurging into the crater. The strongest inward current is more than 200 km/h, and at the front of the leading wave system the outward current is up to 160 km/h. The front of the outward propagating wave is still a breaking bore, about 300 m high.

After 600 s, the water is climbing the central height. The front is no longer breaking and a marked, smooth peak has evolved, with a slightly reduced height of 250 m. This reduction is due to breaking and radial spread, but is counteracted by the growth of the peak (see discussion below). At this time the amplitude-to-depth ratio is 0.63, which is somewhat too high for (and outside the limitation of) the Boussinesq equations. At 800 s, a second peak is visible at the front of the leading wave system. Later, at 1000 s, yet a third peak is discernible and it is apparent that an undular bore is in progress. At this time the leading peak is located 116 km from the impact center. Closer than 20 km to the impact center, another wave elevation is being produced from the resurge.

After 1000 s, the amplitude-to-depth ratio for the leading crest has fallen below 0.5 and it seems reasonable to transfer the tsunami from SOVA to the radial symmetric Boussinesq model using the surface elevation from SOVA (see Figs. 5 and 6). The transfer of velocity into the Boussinesq models are described in Appendix 2, and the depth-averaged potential is found by integrating the velocity determined by Equation 7 (see Appendix 2) found in the same appendix. Direct transfer of fluid velocities from SOVA to the Boussinesq model has also been attempted. However, that resulted in stronger

Table 2. Models applied for the simulation of the tsunami.

Model	Dimensions[a]	Refraction	Defraction	Applied in	Description
Quasi-symmetric ray theory	2-D	–	–	"Qualitative Features—Simplified Computations" section	Appendix 3, Equation 21
Quasi-symmetric Boussinesq	2-D	–	–	"Near-Field Tsunami Evolution" and "Qualitative Features—Simplified Computations" sections	Appendix 1, Equations 1 and 2
Ray theory	3-D	+	–	"Qualitative Features—Simplified Computations" section	Appendix 3, Equations 18 and 19
Boussinesq	3-D	+	+	"Full Boussinesq Simulations" section	Appendix 1, Equations 1 and 2

[a]Physical dimensions; however, the mathematical description is reduced by 1 due to depth-averaged equations.

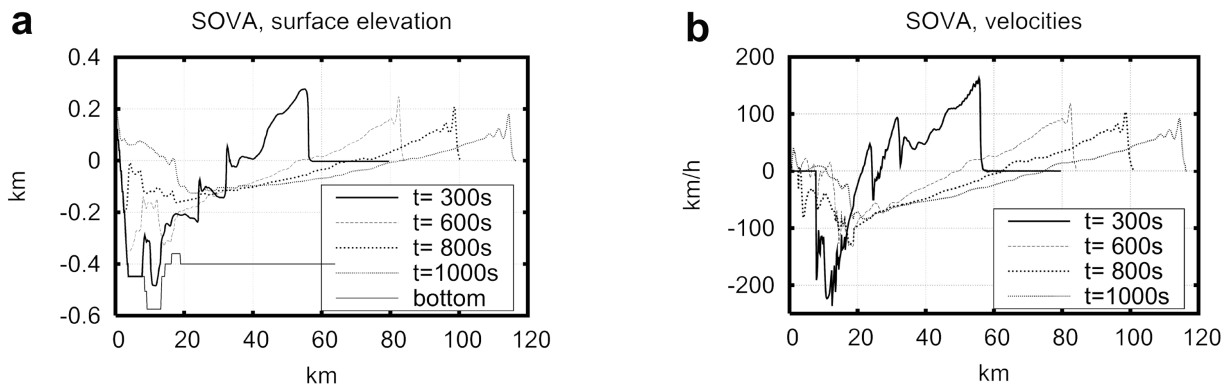

Fig. 4. Surface elevation (a) and depth averaged horizontal velocities (b) after the Mjølnir impact. Simulations based on the SOVA model. The resolutions are Δr = 160 m and Δz = 40 m.

deviations from a purely outgoing wave system due to the different physics in the two models and the coarse resolution in the SOVA model.

We observe that the evolution of the leading wave as an undular bore continues, with an increasing number of apparent peaks (see Figs. 5 and 6). Moreover, in the Boussinesq simulation the amplitude of the leading peaks increases significantly from t = 1000 s and culminates with a maximum at t ~1150 s. This amplification is in agreement with the dynamics of plane undular bores, where the highest peak may reach double the initial amplitude according to long wave theory (Peregrine 1966). Tests with both Boussinesq equations and full potential theory on undular bores from idealized initial states confirm this and also indicate that errors inherent in the Boussinesq model are no more than 10–15%, even when the final wave heights becomes 0.7 times the depth. In the case of radial symmetry, the amplification due to bore dynamics is opposed by the spatial spreading of the wave crest. When individual waves separate the radial spread becomes dominant and the amplitudes start to drop as is seen at t = 1550 s in Fig. 5. The growth in amplitude for t > 1000 s in the Boussinesq simulations seems to contradict the attenuation in the SOVA results for t < 1000 s. Attempts to employ 3-D potential theory for t < 1000 s have not been completely successful, mainly due to under-resolution. However, these simulations combined with the Boussinesq results indicate that there may be too much

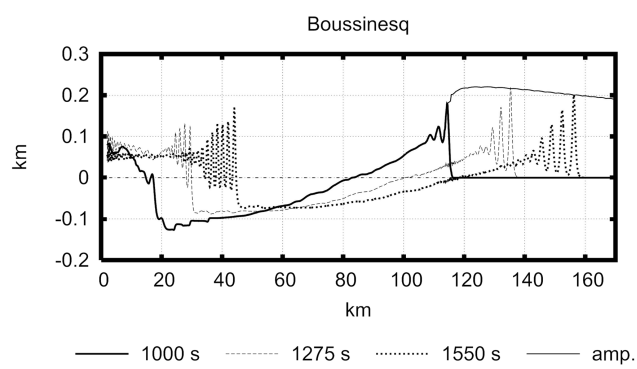

Fig. 5. Surfaces from the Boussinesq model. Resolution: Δr = 50 m, Δt = 0.8 s.

damping in the SOVA model and that the fission process in the undular bore dynamics is too slow. This is not an unexpected effect considering that SOVA includes a solid (crust), liquid (ocean), and vapor (atmosphere) target, and where the coarse resolution necessarily implies a coarse representation of the sea surface. On the contrary, it is impressive that a model of this kind captures the qualitative properties of the undular bore so well. When the individual waves separate, and r becomes large, they should approach solitary waves. This is indeed the case, as demonstrated in Fig. 6, where we observe that the front is quite close to that of a solitary wave of corresponding height already at t = 1000 s.

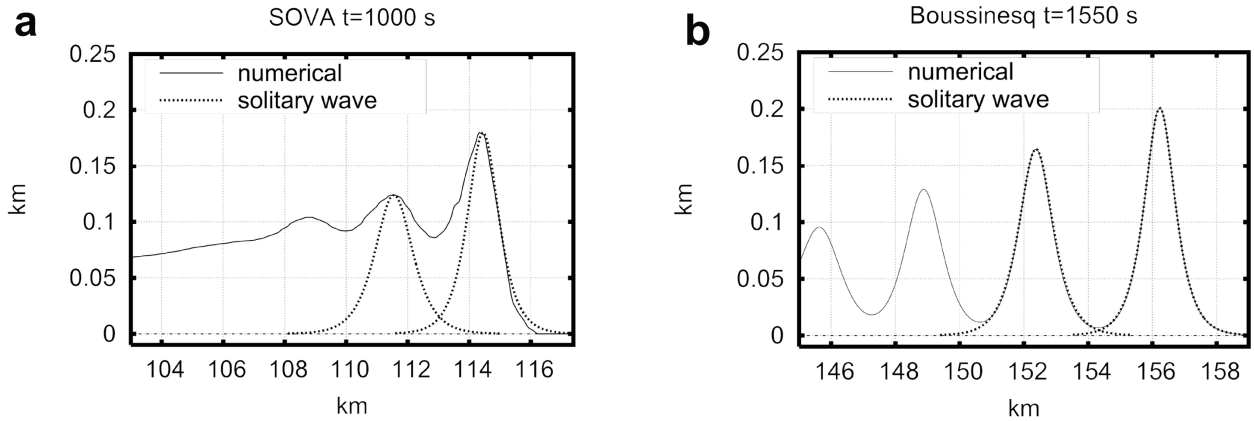

Fig. 6. Separation into solitary waves in the evolution of the Mjølnir tsunami. a) Matching of the SOVA solution at 1000 s to the exact solitary wave solution of Tanaka (1986). b) Numerical Boussinesq solution matched with the corresponding solitary wave solution. The solitary wave solutions are calculated from the maxima of the numerical surfaces and the depth. Resolution: $\Delta r = 50$ m, $\Delta t = 0.8$ s.

According to the Boussinesq solution in Fig. 5, the waves from the resurge of water into the crater develop into a secondary undular bore. It must be noted, however, that these waves are more nonlinear than the leading system due to the intermediate trough. The highest amplitude nearly reaches 0.7 times the depth in front of the system. Hence, breaking cannot be ruled out. Still, as radial dilution takes its toll on the wave heights, it is probable that a smooth undular bore evolves. At later times (see, for instance, Fig. 14), the secondary system is much weaker than the primary one.

The evolution of undular bores and subsequent fission into solitary waves are well established in the literature for plane waves, or radially symmetric waves, propagating in constant depth. Save for the crater, the bottom gradients have been ignored in the simulations described above. In systematic studies on evolution on undular bores in variable depth, we have found that solitary wave-like crests do evolve even in bathymetries with bottom gradients that are an order of magnitude higher than those in the Barents Sea. Then, the variable depth influence is small indeed. Numerical tests indicate errors in amplitude less than 3% for the first 1000 s (using a Boussinesq model initiated by an idealized bore of length 32 km and $A = 240$ m). In subsequent computations we also find that, when generated, the individual waves retain their identity as solitary waves, until they break in shoaling water.

It is reasonable to assume that large marine impacts, producing craters with diameters that are an order of magnitude larger than the water depth, will generate ocean surface waves that are long and strongly nonlinear. In turn, such waves will develop into bores that are either breaking or undular, depending on their amplitudes. The bore will be undular if the initially long, shelf-like wave has a small amplitude (Peregrine 1966). In contrast, a large initial amplitude produces a breaking bore, possibly with some minor undulation in the front that is rapidly consumed by the dissipation in the breaking process. For plane (straight-crested) waves, the limiting initial amplitude is around 0.3–0.4 times the depth, while radial symmetry favors generation of undular bores strongly. Presumably, if the propagation distance is sufficiently large, every bore will eventually be transformed to an undular one when the amplitude is reduced due to radial spreading. We have not performed systematic tests to investigate the likelihood of a modified Mjølnir impact producing a breaking bore some distance from the crater.

In a short paper, Weiss et al. (2003) presented results for a bolide 1 km in diameter with a speed of 12 km/h hitting a 1250 m deep ocean. This corresponds to a bolide-diameter-to-sea-depth ratio that is between those of the Mjølnir and Eltanin cases. An impact model (SALE) was coupled to a nonlinear shallow water model in the far field. After 800 s, a breaking bore of height near 0.3 times the depth was evident 20 km from the impact center. If dispersion had been included in the tsunami propagation model this bore would probably have been transformed into an undular one. Also, after 1700 s, a second tsunami wave system was developing from the resurge into the crater. Even though the parameters are different from the Mjølnir case, some of the important features are similar.

The Eltanin impact has been subject to several studies (e.g., Crawford et al. 1998; Shuvalov 2003; Gisler et al. 2003, 2004). However, since no crater was formed, the characteristics of both the impact and tsunami are very different from the Mjølnir event. For an asteroid 800 m in diameter and an ocean depth of 5000 m, using the SAGE multi-material code, Gisler et al. (2003, 2004) found early wave amplitudes that were much larger (up to 1 km or more) than those of the Mjølnir tsunami. However, the amplitude-to-depth ratio becomes very rapidly smaller in the Eltanin than in the Mjølnir case. Thus, the breaking is more likely to be governed by the amplitude-wavelength ratio typical of deep-water approximation, rather than the amplitude-depth ratio. Moreover, the characteristic wavelengths are not much

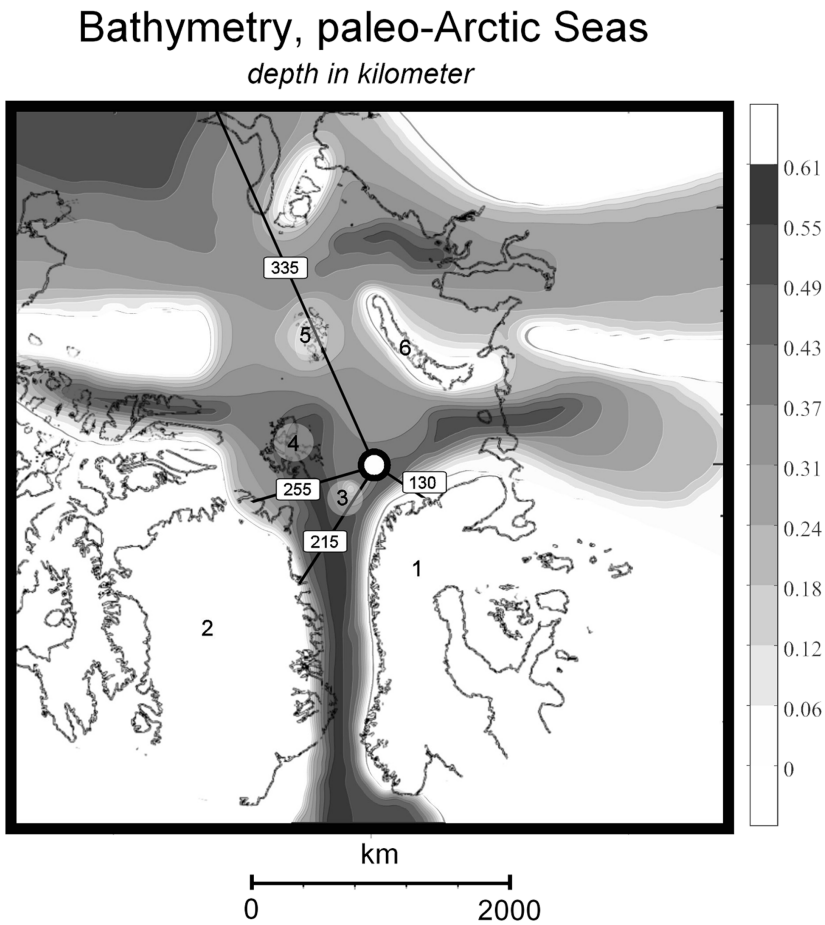

Fig. 7. The reconstructed sea floor topography of the paleo-Arctic Seas at the actual time (approximately 150 million years ago). The impact center is marked with a bullet in the middle of the figure. White areas are land. The black lines out from the impact center are cross sections used in the simulations, and the corresponding labels in the white boxes are the angle in degrees from north. The remaining keys (1–6) are: 1 = Norway/Scandinavia, 2 = Greenland, 3 = pre-Bear Island, 4 = pre-Svalbard, 5 = pre-Franz Josef Land, 6 = Novaya Zemlya. At this time Bear Island (sea mount), Svalbard, and Franz Josef Land were lying under water.

larger than the depths. Hence, the far-field tsunami characteristics are very different from those of the Mjølnir tsunami. The huge coefficients for far-field amplitude attenuation, from Gisler et al. (2003, 2004) were discussed previously in the "Optimal Approximation and Symptotic Behavior in the Far-Field" section. Those papers do not provide sufficient details on the resulting wave forms and it is thus difficult to assess their findings. However, it is improbable that any breaking wave forms could results in such large attenuation coefficients. Hence, we are lead to attribute the damping to either breaking or the employed numerical method. Given that the attenuation appears to be strongest for the smaller asteroid diameters we are inclined toward the latter explanation. Anyhow, the strong damping is not a general characteristic for waves from deep-ocean impacts. This is supported by a recent article (Weiss et al. 2006) where the SALE impact model is combined with a Boussinesq model for deep-water propagation and the well-known tsunami model MOST for run-up. They employed a nonstandard Boussinesq model with anisotropic dispersion. The diameter of the asteroid was 800 m, the ocean depth 5000 m, and the impact velocity 10 km/s, corresponding to a fourth of the kinetic energy in the corresponding simulation by Gisler et al. (2004). At t = 240 s the SALE solution of Weiss et al. (2006) is transferred to the Boussinesq model. At this point the combined length of the first peak and trough is around four ocean depths, which is acceptable for the particular Boussinesq model used in that work. The wave then develops into a linear, dispersive wave system. Unlike in the case of the Mjølnir tsunami, there is no sign of an undular bore or soliton generation in the deep ocean. At later times, the attenuation is reported to be a somewhat larger than r^{-1}. This may be partly due to the initial wave shape in the Boussinesq simulation (see the "Optimal Approximation and Symptotic Behavior in the Far-Field" section). Anyhow, the attenuation found by Weiss et al. (2006) clearly contradicts the huge damping reported by Gisler et al. (2003, 2004). In view of this and the damping found in the SOVA solution

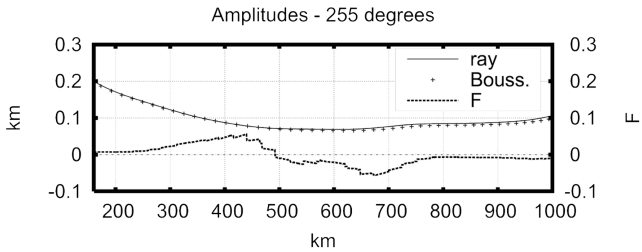

Fig. 8. Comparison of quasi-symmetric solutions of the Mjølnir tsunami between ray theory and Boussinesq. The profile is taken westward in the direction of 255° from north (see Fig. 7). The spatial and time increments are $\Delta r = 100$ m and $\Delta t = 1.6$ s, respectively. F is the validity factor from Equation 23 and refers to the right axis.

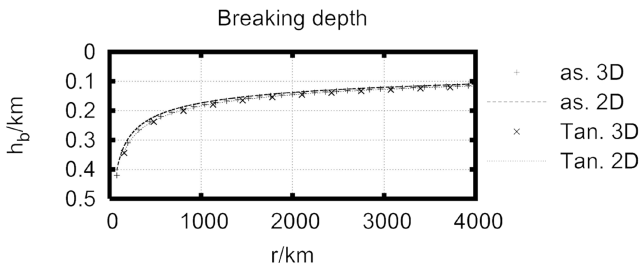

Fig. 10. Comparison of critical depth for breaking, h_b. "Tan." (Tanaka) is given by full potential theory, while "as." is derived from the asymptotic expressions of (21).

described here, we are lead to suggest that general impact codes are not suited for long-term simulations of the tsunami propagation. For smaller diameter-to-depth ratios the generated surface gravity waves are even shorter and will, probably, become dominated by a modulated periodic train as found by Ward and Asphaug (2002). A Boussinesq-type model is then not appropriate.

Tsunami Propagation and Shoaling

The wave models described in Table 2 yield a range of simulation tools that we have used to investigate the propagation of the Mjølnir tsunami. The primary model, though, with limited applicability due to its huge demands of computational resources, is the three-dimensional weakly nonlinear and dispersive Boussinesq equations. As a simple alternative we employ quasi-symmetric solutions where the number of dimensions is reduced by one. By assuming radial symmetry, the equations are solved with the depth $h(r, \theta = C)$ extracted along a straight line from the impact center. The straight line is defined by the angle C. Correspondingly, we have used the ray theory with two horizontal dimensions as well as in the quasi-symmetric fashion by simulating the leading wave of the tsunami along several lines defined by different values of the angle C. Naturally, the real bathymetry is not symmetric and the quasi-symmetric solutions are only approximations. However, they deviate from the full three-

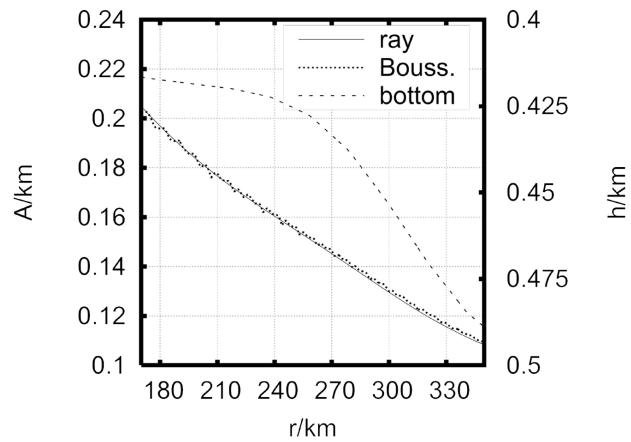

Fig. 9. Amplitude of the leading crest. Comparison of 3-D ray theory (label "ray") and 3-D Boussinesq simulations (label "Bouss.") as explained in the text. The cross section is taken out from the impact center at approximately 255° from the north (see Fig. 7). The resolution for the Boussinesq simulation is $\Delta x = \Delta y = 400$ m and $\Delta t = 6.3$ s, while for the three-dimensional ray theory we have used $\Delta\theta = 2\pi/100$ and $\Delta t = 3.2$ s.

dimensional solutions by less than 1% within distances of 500 km, with the exception of the direction toward paleo-Norway. For larger distances effects of refraction and diffraction, which are not contained in the quasi-symmetric equations, become important.

We have reconstructed the bathymetry of the paleo-Arctic Seas based on our own field work and regional compilations as shown in Fig. 7, which also show the positions of today's coastlines. Based on sedimentological and paleontological information, at the time of the impact the paleo-Arctic Seas were dominated by shallow water (~200–600 m) with the deepest part between paleo-Norway and paleo-Greenland.

Qualitative Features—Simplified Computations

The starting point for the optical (ray) theory is set after the leading solitary wave has emerged. We use the position $r_0 = 160$ km from the impact center, the amplitude $A_0 = 200$ m, and depth $h_0 = 400$ m. Only the leading crest will be computed by ray theory. We could also have employed the optical theory to the following crests as soon as they become separated, and in the absence of interference with reflections from land. However, the highest amplitude is associated with the leading crest.

In Fig. 8, we verify the quasi-symmetric ray theory by comparing the results with a simulation using the quasi-symmetric Boussinesq model. For the chosen typical depth profile, the agreement is very good. As long as the depth gradients and thereby the error factor F are small, there are no discernible differences between the Boussinesq and ray theory solutions. However, when the wave crosses regions with a larger F, small errors in the wave theory, presumably

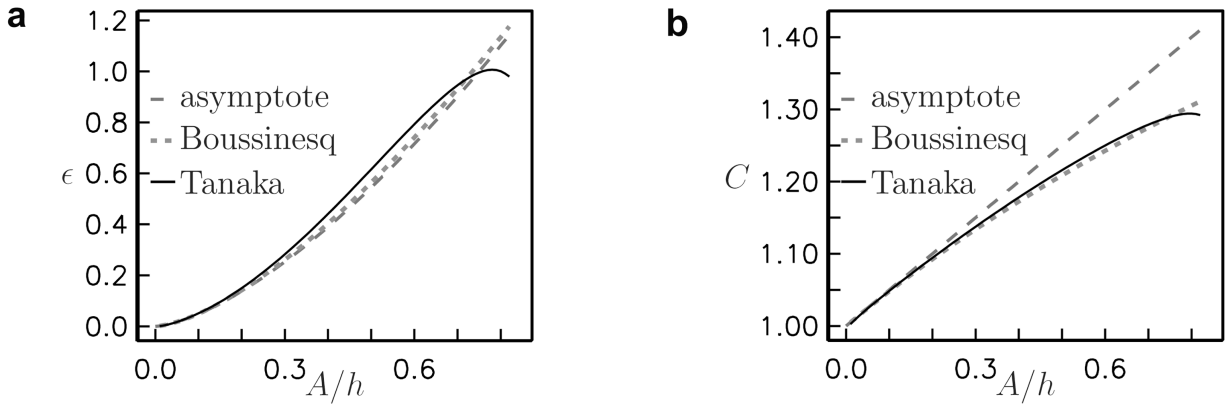

Fig. 11. Energy densities (a) and wave celerities (b) for solitary waves. Asymptotic relations for $A/h << 1$, relations for Boussinesq equations, and from Tanaka's method, as explained in the text.

due to nonlinear diffraction, accumulate to yield minor discrepancies. A corresponding comparison with two horizontal dimensions is given in Fig. 9. The depicted cross section is taken westward from the impact center.

The first application of the quasi-symmetric ray theory is in estimating the depth at which breaking first occurs under shoaling. Using the asymptotic expression for the amplitude found in Equation 21 of Appendix 3 with $A/h = 0.72$ (3-D) and 0.78 (2-D) as critical values, we find the critical depth for breaking, h_b, as a function of distance from the impact center. Figure 10 shows that the breaking depth is rather similar for the two breaking limits. Furthermore, h_b from the asymptotic expression for ε (see Equation 16 in Appendix 3) follows the h_b from the corresponding full relation (from the full potential theory of Tanaka) closely. We presumably owe this to the moderate differences between the various approximations for ε, as shown in Fig. 11. In particular, the asymptotic and Tanaka curves intersect near the critical amplitude, due to the maximum at $A = 0.78$ h in the latter curve. This indicates that the onset of breaking, in the meaning $A/h > 0.72$, may be well predicted by Boussinesq-type equations. Figure 12 shows the critical depth for breaking, together with some depth profiles from the paleo-bathymetry along different direction through the impact center. At distances as large as 2000 km, the tsunami still will break at depths close to 150 m. Toward paleo-Norway (130°, see Fig. 7), we must expect breaking at a depth of 300 m, approximately 120 km off the coast. The tsunami will be breaking over the pre-Bear Island and pre-Franz Josef Land regions (in the directions 215 and 335 degrees, respectively). At Greenland (255°) breaking occurs at a depth of 185 m about 1040 km from the impact center.

Combining the quasi-symmetric ray theory in many directions, we obtain the amplitude distribution in Fig. 13. It is observed that breaking is confined to the shoals and the coast. We have also computed the Mjølnir tsunami with today's bathymetry (results not shown). In this case, the deeper parts of the Barents Sea, south of Bear Island, were the

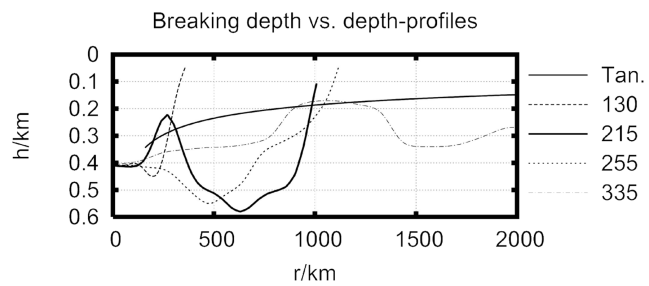

Fig. 12. Critical depth for breaking, h_b, of the Mjølnir tsunami plotted against some depth profiles taken from the paleo-bathymetry. The label for the radial depth profiles reflects the degrees of the direction out from the impact center (see Fig. 7). Towards Greenland (in the direction of 215°) the pre-Bear Island area is found 280 km from the impact center, while in the direction of 335° the pre-Franz Josef Land region is located at 1100 km.

only nonbreaking regions close to the impact. Another noteworthy feature of the present bathymetry is the deep sea basins westward and northward of the impact site. In these directions, the optics was inadequate to describe the transition of the solitary waves over the continental margins. Due to too-steep bottom gradients the solitary waves lose their identity and are transformed to dispersive linear wave fronts.

Naturally, the quasi-symmetric ray theory cannot include refraction of waves. Using the three-dimensional ray theory we may simulate the general evolution of the crest with the inclusion of wave refraction as well. When there is a point of a crest that touches land, or where breaking should have occurred, ray theory fails locally. Due to the nonlinear refraction the errors are then transported along the crest as progressive modulations. For a nearly straight crest, the asymptotic ($A/h \to 0$) crosswise celerity is $\sqrt{gA/3}$ (Miles 1977; Pedersen 1994), which corresponds to 65 km/h for $A = 100$ m. If the depth is 400 m, then a localized disturbance of the crest will influence a sector of 30° downstream. The result is that the parts of the crest adjacent to a local failure of ray theory will also be corrupted. Naturally, the same crosswise

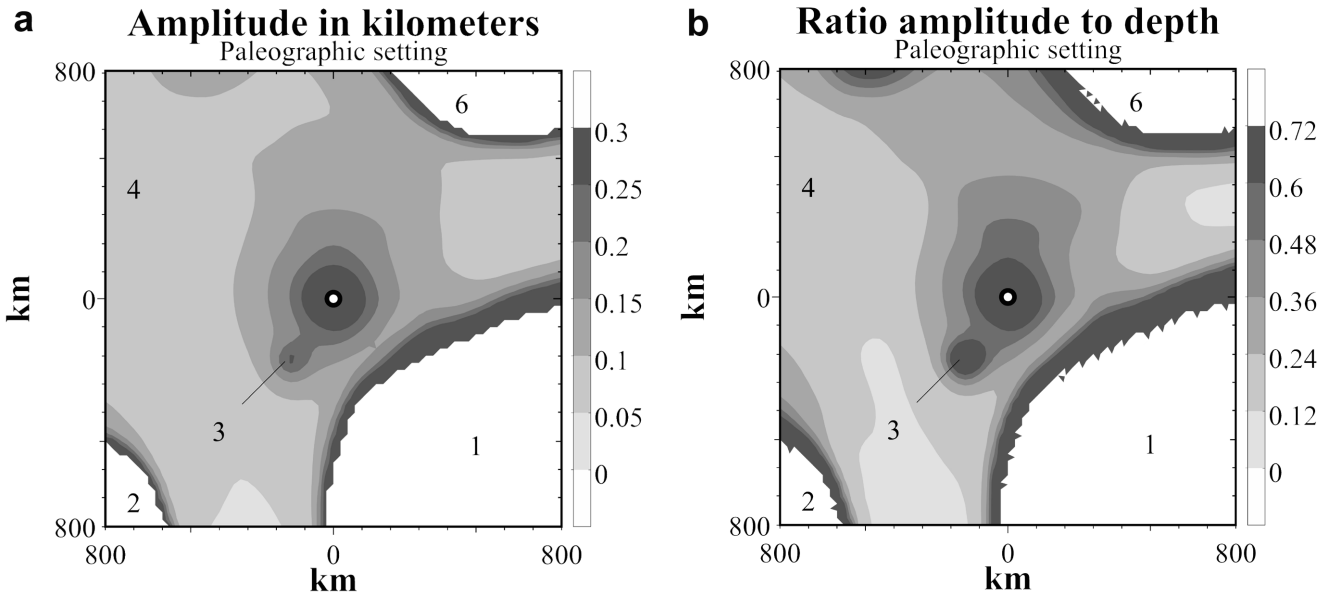

Fig. 13. Amplitude (a) and ratio amplitude to depth (A/h) (b) estimated by quasi-symmetric ray theory as explained in the text. Amplitudes above 0.3 km and values of A/h over the breaking criterion 0.72 are truncated. (See Fig. 7 for explanation of the key numbers.)

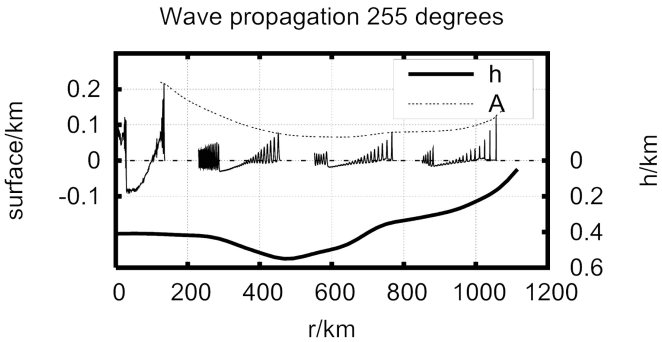

Fig. 14. Quasi-symmetric solutions of wave propagation with depth profile extracted from the impact center toward paleo-Greenland (255°; see Fig. 7). The solutions are printed at t = 23 min, 1 h 33 min, 2 h 45 min, and 4 h 6 min, respectively. Only the primary wave system and the leading part of the secondary wave system are plotted. The spatial and time increments are Δr = 100 m and Δt = 1.6 s. The corresponding close-ups of the front of the first system are given in Fig. 15.

spread of local changes on a crest, physical or unphysical, will appear in full solutions of the Boussinesq equations.

The results of quasi-symmetric Boussinesq simulations toward paleo-Greenland are displayed in Fig. 14. Both the leading and the secondary (only the front shown) wave systems form distinct trains of solitary waves. During the tsunami propagation the minimum amplitude is about 60 m, but when the waves approach land the amplitudes pick up again. In Fig. 15, more details of the leading part of the solutions are depicted.

After 4 h, the leading solitary wave has slightly exceeded the theoretical threshold for breaking (α = 0.72) at r ~1060 km (distance from impact) and for a depth h = 170 m, which agrees with the theoretical breaking depth shown in Fig. 12. We also observe that the resolution at this point is coarse relative to the wavelength. The wave speed is ranging from 190 to 280 km/h throughout the simulation, while the depth-averaged particle speed varies from 35 to ~100 km/h. Applying the relation between the depth-averaged velocity and the velocity at the sea bottom found in Appendix 2, we find that the particle velocity at the bottom generally is above 90% of the depth-averaged value.

Numerical tests with a quasi-symmetric Boussinesq model indicate that a resolution of $\Delta x = \Delta y = h$ is fairly appropriate for solitary waves with an amplitude-to-depth ratio up to 0.4 (see Fig. 16). The depth profile in the figure runs from the impact center towards paleo-Norway in the direction of 130°, as indicated in Fig. 7. During shoaling, the solitary waves become shorter and more poorly resolved. As a consequence the amplification is under-represented.

Full Boussinesq Simulations

In the full-scale simulations using a three-dimensional version of the Boussinesq model, we consider a domain of 800 × 800 km around the impact center. As previously described, the Mjølnir impact generated an undular bore which developed into a train of solitary waves. Typical length of the leading solitary wave at depths of 400 m is a few kilometers, which is much shorter than typical wavelengths of seismic tsunamis in corresponding depths. Hence, the main challenge in the present simulations compared to those of earthquake-generated tsunamis is the need for very high resolution and nonlinear as well as dispersive equations throughout the whole computational

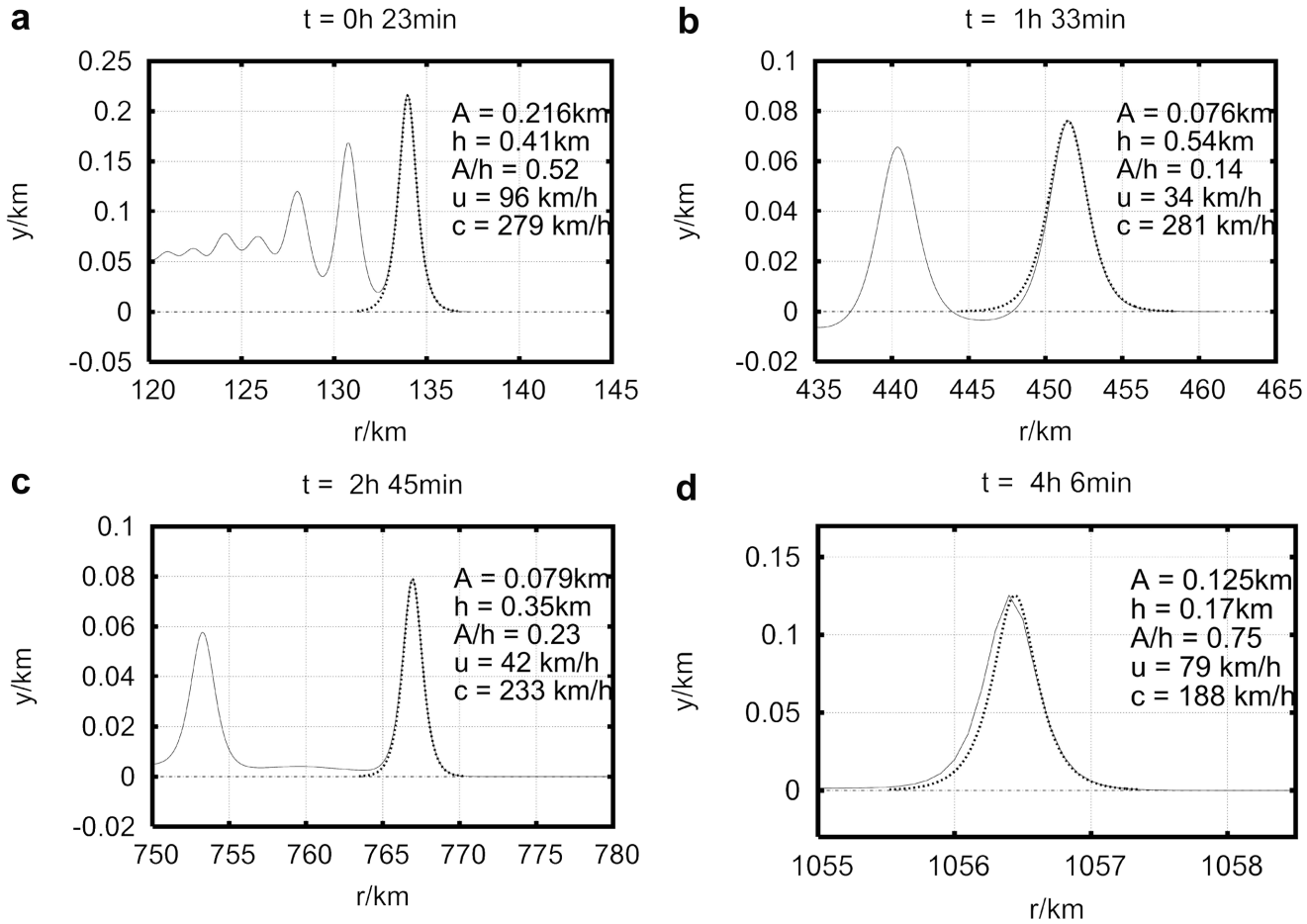

Fig. 15. Front of leading wave system for the quasi-symmetric Boussinesq solutions shown in Fig. 14. The first crest of the simulation (solid line) is compared to a solitary wave (dashed line) scaled by the amplitude and water-depth under the crest. r is the distance, A the amplitude of the leading crest, h is the water depth, u the particle velocity, and c the wave speed.

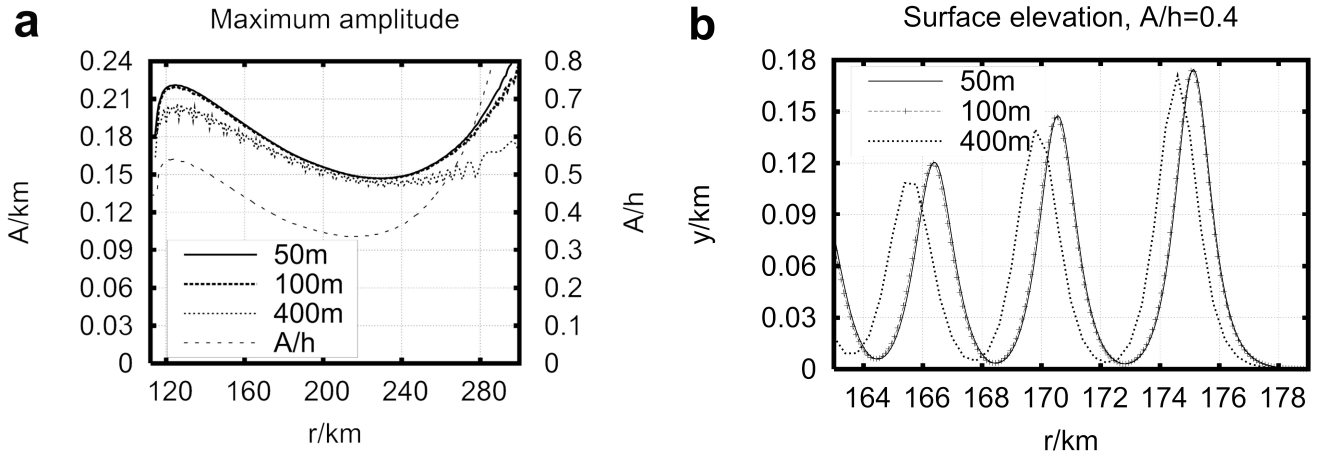

Fig. 16. Convergence tests for quasi-symmetric Boussinesq simulations. The labels are spatial increments in meters (Δr). The convergence is shown as amplitude tracking (a) and snapshot of the surface at t = 23 min (b). The time increments (Δt) are 6.3 s, 1.6 s, and 0.8 s, with corresponding spatial increments of 400 m, 100 m, and 50 m, respectively ($t \in$ [17 min, 90 min]). In (a) the ratio amplitude to depth (label "A/h") refers to the right axis.

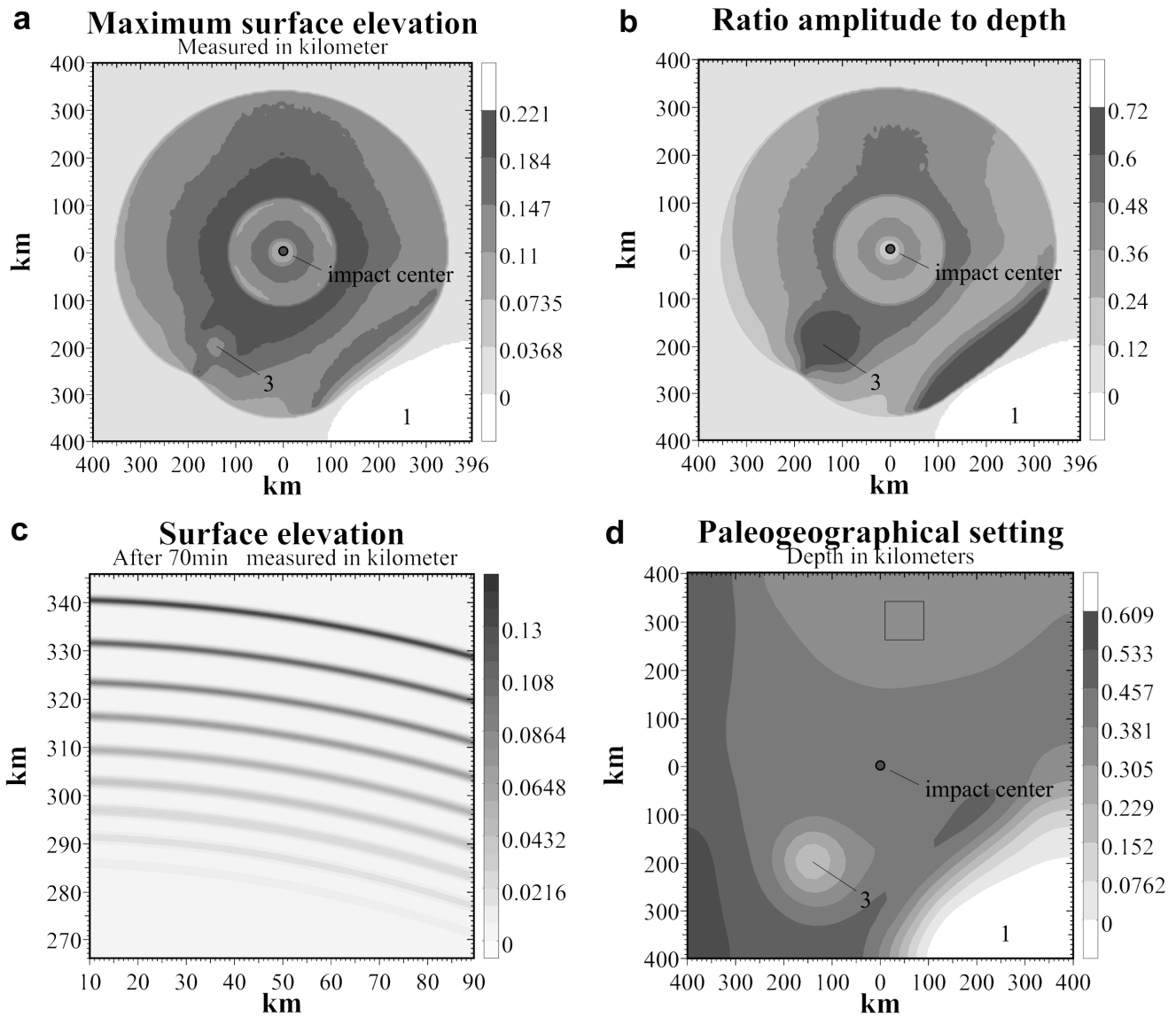

Fig. 17. Simulations using the reconstructed paleography/paleo-bathymetry and the three-dimensional Boussinesq equations. Panel (a) shows the maximum surface elevation and (b) shows the maximum amplitude-to-depth ratio during the tsunami propagation from t = 17 min to 1 h 10 min. Panel (c) shows a local part of the solution. The plotting area is indicated with a rectangle in (d) where we have plotted the bathymetry applied in the simulations. Note that values of $A/h > 0.72$ are truncated. The resolutions are $\Delta x = \Delta y = 0.4$ km and $\Delta t = 6.3$ s. (See Fig. 7 for explanation of the key numbers.)

domain. The simulations presented below in a rather small domain have 4 million nodes corresponding to a resolution of $\Delta x = \Delta y = 400$ m, which is reasonable but somewhat coarse in view of the grid refinement tests shown in Fig. 16. The simulations are run on eight nodes of a parallel Linux cluster.

Figure 17 summarizes some of the results from three-dimensional simulations. After 1 h and 10 min, the leading waves are completely separated into solitary waves (see lower left panel). Here the leading crest is about 144 m high and the five first waves are all above 50 m. The overall maximum amplitude during the whole simulation is up to 220 m (upper left panel). See also the cross sections of the surface elevation in Fig. 18. The breaking feature in our model has been activated over pre-Bear Island area and toward paleo-Norway at depths less than approximately 310 and 260 m, respectively (upper left panel). These depths are slightly less than the predicted breaking depth due to under-resolution in the Boussinesq model. In the upper left panel the breaking is shown as reduced amplitude (see, e.g., over pre-Bear Island).

The breaking feature in our Boussinesq model reduces the amplitude in breaking areas. Figure 18 shows cross sections of breaking solutions taken along a line from the

impact center toward Norway. After 1 h there is no breaking, but after 1 h and 10 min, the front of the solutions is significantly reduced by breaking (spilling) and the wave crests above the critical value of *A/h* are damped as they enter shallower water.

CONCLUDING REMARKS

In this paper, we have modeled the generation and the propagation of the tsunami caused by the Mjølnir impact about 142 million years ago. The tsunami generation phase is modeled by the multi-material code SOVA, while the tsunami propagation within the limitations of shallow water theory is modeled by combining the weakly dispersive and nonlinear Boussinesq equations and ray theory.

In the numerical simulations we have seen that both the generation and propagation are strongly influenced by nonlinearities. A few minutes after the impact, the tsunami starts to develop as an undular bore, which then develops into a train of solitary waves. The wave characteristics are due to genuine nonlinear and dispersive features, but neither shallow water models nor linear theory can capture them. Unlike traditional shallow water models, nonlinear and dispersive equations lead to an implicit system of unknowns. In three-dimensional simulations this implicitness and the need of high resolution due to short waves (1–4 km) give a computationally heavy problem, even for a rather small domain. In this paper, we have applied numerical simulations using the power of the combination of a domain decomposition method and parallel computing. Moreover, important qualitative information, such as regions of breaking, is obtained by simplified techniques that include quasi-symmetric simulations and ray theory for solitary waves. The quasi-symmetric approximation is accurate until diffraction/refraction due to land or particularly distinct shoals, such as the pre-Bear Island, become important. Ray theory is seldom applied to solitary waves, but in the present case this simple approach provides useful results both as asymptotic results in closed form and computations. The optical theory may be useful also for related cases where undular bores are produced by seismic tsunami, or tides, in estuaries and shallow straits.

The total energy in the Mjølnir tsunami is several orders of magnitude larger than the energy of the disastrous Indian Ocean tsunami of 2004. This work shows that the impact caused amplitudes above 200 m, and in some cases the amplitude is still above 100 m after 4 h. Due to these high amplitudes the tsunami will break far from the coastline. For instance, the tsunami traveling toward paleo-Norway should break at a depth of around 300 m and 120 km offshore.

At the time of impact, the sea bed was sedimented by organic rich mud and clays that presumably were unconsolidated. Hence, there was no well-defined sea bottom, but a thick (turbid) layer with gradually increasing density downward. Then, the tsunami, causing repeated current pulses with particle velocities in the range of 30–90 km/h close to the sea floor, must have generated substantial mixing and consequently reworked the sea floor dramatically. A total change of the marine environment throughout the paleo-Barents Sea is thus likely. The direct effect of the re-sedimentation is difficult to detect in the layers, but the bloom of the green algae (*Leiosphaerida*) (Dypvik et al. 2004b; Smelror et al. 2005) surely indicate the environmental changes. It is also possible that the unconsolidated bottom and the suspended fine-grained sediments caused a substantial damping of the tsunami. Similar effects may be important for seismic tsunamis and storm surges flooding tidal flats and entering estuaries and other shallow regions that are rich in sediments. However, we expect that of the entire paleo-Barents Sea region, the clearest evidence of tsunami today should come from the coastal regions.

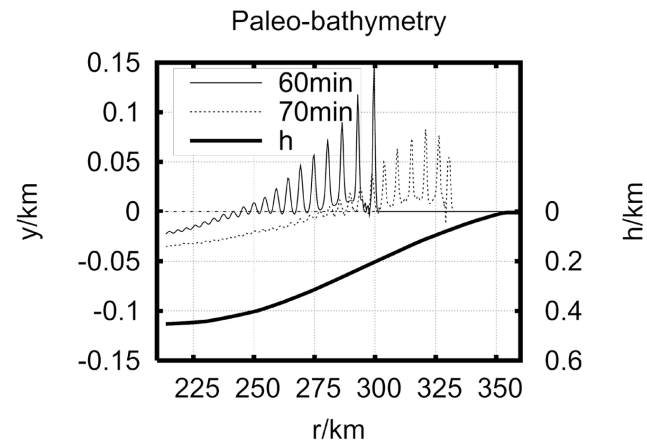

Fig. 18. Breaking of the train of solitary waves towards Norway. The profiles are cross sections in the three-dimensional fields after 60 and 70 min. The thick black curve is the sea bottom, *h* (depth in kilometers shown at right vertical axis). The lower axis is the distance from impact center, and waves are travelling to the right.

In this work we have focused on the generation, propagation, and shoaling of the Mjølnir tsunami. While the important investigations regarding the run-up of the tsunami are rather complex and require further analysis.

Acknowledgments–The authors are grateful to Øyvind Kristiansen for his efforts with checking the validity of the long wave models. The authors also wish to thank Don Korycansky, Kai Wünnemann, and Betty Pierazzo for their many insightful comments. The work has been supported by the Research Council of Norway under grant no. 154831. The present article is contribution no. 103 of the International Centre for Geohazards (ICG).

Editorial Handling—Dr. Elisabetta Pierazzo

REFERENCES

Artemieva N. A. and Shuvalov V. V. 2002. Shock metamorphism on the ocean floor (numerical simulations). *Deep Sea Research II* 4: 959–968.

Bourgeois J., Hansen T. A., Wiberg P. L., and Kauffman E. G. 1988. A tsunami deposit at the Cretaceous-Tertiary boundary in Texas. *Science* 241:567–570.

Cai X., Acklam E., Langtangen H. P., and Tveito A. 2003. Parallel computing in Diffpack. In *Advanced topics in computational partial differential equations—Numerical methods and Diffpack programming,* edited by Langtangen H. P. and Tveito A. Berlin: Springer. pp. 1–56.

Clarisse J.-M., Newman J. N., and Ursell F. 1995. Integrals with a large parameter: Water waves on finite depth due to an impulse. *Proceedings of the Royal Society A* 450:67–87.

Clamond D. and Grue J. 2001. A fast method for fully nonlinear water wave computations. *Journal of Fluid Mechanics* 447:337–355.

Crawford D. A. and Mader C. L. 1998. Modeling asteroid impact and tsunami. *Science of Tsunami Hazards* 16:21–30.

Dold J. W. 1992. An efficient surface-integral algorithm applied to unsteady gravity waves. *Journal of Computational Physics* 103: 90–115.

Dypvik H., Gudlaugsson S. T., Tsikalas F., Attrep M., Jr., Ferrell R. E., Jr., Krinsley D. H., Mørk A., Faleide J. I., and Nagy J. 1996. Mjølnir structure: An impact crater in the Barents Sea. *Geology* 24:779–782.

Dypvik H. and Jansa L. 2003. Sedimentary signatures and processes during marine bolide impacts: A review. *Sedimentary Geology* 161:308–341.

Dypvik H., Burchell M., and Claeys P. 2004a. Impacts into marine and icy environments—A short review. In *Cratering in marine environments and on ice,* edited by Dypvik H., Burchell M., and Claeys P. Heidelberg: Springer-Verlag. pp. 1–20.

Dypvik H., Sandbakken P. T., Postma G., and Mørk A. 2004b. Post-impact sedimentation in the Mjølnir crater. *Sedimentary Geology* 168:227–247.

Dypvik H., Wolbach W. S., Shuvalov V., and Weaver S. L. W. Forthcoming. Did the Mjølnir asteroid impact ignite Barents Sea hydrocarbon source rocks? *Geological Society of America*.

Fructus D., Clamond D., Grue J., and Kristiansen Ø. 2005. An efficient model for three-dimensional surface wave simulations: Part I: Free space problems. *Journal of Computational Physics* 205:665–685.

Gault D. E. and Sonett C. P. 1982. Laboratory simulation of pelagic asteroidal impact: Atmospheric injection, benthic topography, and the surface wave radiation field. In *Geological implications of impacts of large asteroids and comets on the Earth,* edited by Silver L. T. and Schultz P. H. GSA Special Paper #190. Boulder, Colorado: Geological Society of America. pp. 69–92.

Gersonde R., Deutsch A., Ivanov B. A., and Kyte F. T. 2002. Oceanic impacts—A growing field of fundamental science. *Deep Sea Research II* 49:951–957.

Gisler G., Weaver R., Mader C., and Gittings M. 2003. Two- and three-dimensional simulations of asteroid ocean impacts. *Science of Tsunami Hazards* 21:119–134.

Gisler G. R., Weaver R. P., Mader C. L., and Gittings M. L. 2004. Two- and three-dimensional asteroid impact simulations. *Computing in Science and Engineering* 6:46–55.

Grieve R. A. F., James R., Smit J., and Terriault A. 1995. The record of terrestrial impact cratering. *GSA Today* 5:193–196.

Grue J. 2002. On four highly nonlinear phenomena in wave theory and marine hydrodynamics. *Applied Ocean Research* 24:261–274.

Gudlaugsson S. T. 1993. Large impact crater in the Barents Sea. *Geology* 21:291– 294.

Kataoka T. and Tsutahara M. 2004. Transverse instability of surface solitary waves. *Journal of Fluid Mechanics* 512:211–221.

Kennedy A. B., Chen Q., Kirby J. T., and Dalrymple R. A. 2000. Boussinesq modeling of wave transformation, breaking, and run-up. Part I: 1D. *Journal of Waterwaves, Port, Coastal, and Ocean Engineering* 126:39–47.

Ko K. and Kuehl H. H. 1978. Korteweg-de Vries soliton in a slowly varying medium. *Physical Review Letters* 40:233–236.

Korycansky D. G. and Lynett P. J. 2005. Offshore breaking of impact tsunami: The Van Dorn effect revisited. *Geophysical Research Letters* 32, doi:10.1029/2004GL021918.

Kulikovskii A. G. and Reutov V. A. 1976. Movement of solitary and periodic waves with an amplitude close to the limiting in a liquid layer of slowly varying depth. *Fluid Dynamics* 11:884–893.

Kyte F., Zhou Z., and Wasson J. T. 1981. High noble metal concentrations in a late Pliocene sediment. *Nature* 292:417–420.

Langtangen H. P. and Pedersen G. 1998. Computational models for weakly dispersive nonlinear water waves. *Computer Methods in Applied Mechanics and Engineering* 160:337–358.

Lynett P. J., Wu T.-R., and Liu P. L.-F. 2002. Modeling wave run-up with depth-integrated equations. *Coastal Engineering* 46:89–107.

Mei C. C. 1989. *The applied dynamics of ocean surface waves*. London: World Scientific. 740 p.

Miles J. W. 1977. Diffraction of solitary waves. *Journal of Applied Mathematics and Physics* 28:889–902.

Miles J. W. 1980. Solitary waves. *Annual Review of Fluid Mechanics* 12:11–43.

Pedersen G. 1994. Nonlinear modulations of solitary waves. *Journal of Fluid Mechanics* 267:83–108.

Pedersen G. 1996. Refraction of solitons and wave jumps. In *Waves and nonlinear processes in hydrodynamics,* edited by Gjevik B., Grue J., and Weber J. E. Dordrecht, The Netherlands: Kluwer Academic Publishers. pp. 139–150.

Pedersen G. 2005. Variable depth and the validity of Boussinesq-type models. Preprint Series in Mechanics and Applied Mathematics, vol. 2005, no. 2. Oslo, Norway: Department of Mathematics, University of Oslo, Norway.

Peregrine D. H. 1966. Calculations of the development of an undular bore. *Journal of Fluid Mechanics* 25:321–330.

Peregrine D. H. 1976. Interaction of water waves and currents. *Advances in Applied Mechanics* 16:10–117.

Reutov V. A. 1976. Behaviour of perturbations of solitary and periodic waves on the surface of a heavy liquid. *Fluid Dynamics* 11:778–781.

Russel J. S. 1845. Report on waves. Report of the 14th Meeting of the British Association for the Advancement of Science, York, September 1844 (London 1845). pp. 311–390, plates XLVII–LVI.

Shuvalov V. V., Artemieva N. A., and Kosarev I. B. 1999. 3-D hydrodynamic code SOVA for multimaterial flows, application to Shoemaker Levy 9 comet impact problem. *International Journal of Impact Engineering* 23:847–858.

Shuvalov V. V., Dypvik H., and Tsikalas F. 2002. Numerical simulations of the Mjølnir marine impact crater. *Journal of Geophysical Research* 107, doi:10.1029/2001JE001698.

Shuvalov V. V. 2003. Numerical modeling of the Eltanin impact (abstract #1101). 34th Lunar and Planetary Science Conference. CD-ROM.

Shuvalov V. and Dypvik H. 2004. Ejecta formation and crater development of the Mjølnir impact. *Meteoritics & Planetary Science* 39:467–479.

Smelror M., Kelly R. A., Dypvik H., Mørk A., Nagy J., and

Tsikalas F. 2001. Mjølnir (Barents Sea) meteorite impact ejecta offers a Volgian-Ryazanian boundary marker. *Newsletter on Stratigraphy* 38:129–140.

Smelror M. and Dypvik H. 2005. The sweet aftermath: Environmental changes and biotic restoration following the marine Mjølnir impact (Volgian-Ryazanian boundary, Barents shelf). In *Biological processes associated with impact events,* edited by Cockell C. S., Koeberl C., and Gilmour I. Berlin: Springer. pp. 144–175.

Smit J., Roep T. B., Alvarez W., Montanari A., Claeys P., Grajales-Nishimura J. M., and Bermudez J. 1996. Clastic sandstone complex at the K/T boundary around the Gulf of Mexico: Deposition by tsunami waves induced by the Chicxulub impact? GSA Special Paper #307. Boulder, Colorado: Geological Society of America. pp. 151–182.

Synolakis C. E. and Skjelbreia J. E. 1993. Evolution of maximum amplitude of solitary waves on plane beaches. *Journal of Waterway, Port, Coastal, and Ocean Engineering* 119:323–342.

Tanaka M. 1986. The stability of solitary waves. *Physics of Fluids* 29: 650–655.

Tsikalas F., Gudlaugsson S. T., and Faleide J. I. 1998. The anatomy of a buried complex impact structure: The Mjølnir structure. *Journal of Geophysical Research* 103:30,469–30,484.

Tsikalas F. 2004. Mjølnir crater as a result of an oblique impact: Asymmetry evidence constrains impact direction and angle. In *Impact studies (impact tectonism),* edited by Henkel H. and Koeberl C. Berlin-Heidelberg: Springer. pp. 285–306.

USGS. (U.S. Geological Survey). http://www.usgs.gov. Accessed 11 May 2006.

Van Dorn W. G., Le Méhauté B., and Hwang L.-S. 1968. Handbook of explosion-generated water waves. Report #TC-130, Tetra Tech Inc., Pasadena, California.

Ward S. N. and Asphaug E. 2000. Asteroid impact tsunami: A probabilistic hazard assessment. *Icarus* 145:64–78.

Ward S. N. and Asphaug E. 2002. Impact tsunami—Eltanin. *Deep Sea Research II* 49:1073–1080.

Weiss R., Wünnemann K., and Bahlburg H. 2003. Oceanic impacts, tsunamis, and the influence of the water depth on the quantity and characteristics of the generated waves (abstract #4081). Third International Conference on Large Meteorite Impacts. CD-ROM.

Weiss R., Wünnemann K., and Bahlburg H. 2006. Numerical modeling of generation, propagation, and run-up of tsunamis cause by oceanic impacts: Model strategy and technical solutions. *Geophysical Journal International* 167:77–88.

Wolbach W. S., Widicus S., and Dypvik H. 2001. A preliminary search for evidence of impact-related burning near the Mjølnir impact structure, Barents Sea (abstract #1332). 32nd Lunar and Planetary Science Conference. CD-ROM.

Zelt J. A. 1991. The run-up of nonbreaking and breaking solitary waves. *Coastal Engineering* 15:205–246.

APPENDIX 1: MODELS FOR TSUNAMI PROPAGATION

For tsunami propagation we employ a set of Boussinesq equations that is based on the averaged velocity potential ϕ and the surface elevation η:

$$\frac{\partial\phi}{\partial t} = \frac{1}{2}(\nabla\phi)^2 + g\eta - \frac{1}{2}h\nabla\cdot\nabla\left(h\frac{\partial\phi}{\partial t}\right) + \frac{1}{6}h^2\nabla^2\frac{\partial\phi}{\partial t} = 0 \quad (1)$$

$$\frac{\partial\eta}{\partial t} = -\nabla\cdot\left[(h+\eta)\nabla\phi + h\left(\frac{1}{6}\frac{\partial\eta}{\partial t} - \frac{1}{3}\nabla h\cdot\nabla\phi\right)\nabla h - \vec{D}\right] \quad (2)$$

where g is the acceleration of gravity and $\vec{D}$ is an artificial diffusion term that enable a rough representation of breaking waves. Usually this kind of term is added to the momentum equation. However, when the momentum conservation is represented by the potential in a Bernoulli type of equation, this causes difficulties with both momentum conservation and numerical performance. Naturally, the term may equally well appear in the continuity equation as long as mass conservation is observed. The term reads:

$$\vec{D} = \beta\nabla\eta \quad (3)$$

The determination of an appropriate diffusion factor, β, is far from straightforward and there is presumably no single choice that is universal in the sense that it fits all purposes. Herein, the diffusion is designed to check the growth of solitary waves during shoaling, after they reach a threshold of the ratio amplitude to depth $A/h = \alpha = 0.72$. (The solitary wave solution is discussed in Appendix 3.) Hence, β is zero for $\eta/h < \alpha$. To assign a value to β when the threshold is surpassed we have studied the "post-breaking" behavior for different β in a typical depth profiles from the Barents Sea. It turned out that for a value close to $\beta = 1$ the amplitude-to-depth ratio remained below 0.8 for at least $h > 100$ m. For gentle spilling this is a reasonable behavior, and we thus have employed $\beta = 1$ for active diffusion in all our Boussinesq simulations. However, we do remark that the resulting diffusion will become more and more inappropriate as the shape of the wave is transformed to become substantially different from that of a solitary wave (see the discussion at the end of Appendix 3). Our diffusion term is similar to those employed by Zelt (1991) and Kennedy et al. (2000) where the threshold for α is linked to gradients, but still corresponds to a solitary wave of limiting height. That method with $\alpha = 0.65$ was used to reproduce bores from experiments very well (Kennedy et al. 2000; Lynett et al. 2002). This value of α is a little below the theoretical breaking limits $\alpha = 0.72$ (Kataoka et al. 2004) for the 3-D case and $\alpha = 0.78$ (Tanaka 1986) for plane waves. While the referenced breaking models dissipate energy mainly in a front region, the present extends the dissipative region beyond the peak, which is more reasonable for a spilling breaker.

For the radially symmetric case, Equations 1 and 2 reduce to:

$$\frac{\partial\phi}{\partial t} = \frac{1}{2}\left(\frac{\partial\phi}{\partial r}\right)^2 + g\eta - \frac{1}{2}\frac{h}{r}\frac{\partial}{\partial r}\left(rh\frac{\partial^2\phi}{\partial t\partial r}\right) + \frac{1}{6}\frac{h^2}{r}\frac{\partial}{\partial r}\left(r\frac{\partial^2\phi}{\partial t\partial r}\right) = 0 \quad (4)$$

$$\frac{\partial n}{\partial t} = -\frac{1}{r}\frac{\partial}{\partial r} \cdot$$
$$\left[r(h+\eta)\frac{\partial \phi}{\partial r} + rh\left(\frac{1}{6}\frac{\partial \eta}{\partial t} - \frac{1}{3}\frac{\partial h}{\partial r}\frac{\partial \phi}{\partial r}\right)\frac{\partial h}{\partial r} - D_r\right] \quad (5)$$

Equations 1–2 and 4–5 are well suited for discretization by finite difference and element techniques. We have observed artificial behavior in the presence of extreme bottom gradients in both formulations 1–2 and 4–5. Still, since we have a low-profile bathymetry, no such problems are encountered in the Mjølnir simulations. The sets 1–2 and 4–5 are solved by finite element and finite difference methods very similar to those described in Langtangen et al. (1998). The solver for 1–2 is also parallelized using a data decomposition technique on the linear system level as explained in (Cai et al. 2003).

It turns out that the surface gravity waves from the impact undoubtedly stretch the validity of the Boussinesq-type long wave models concerning height and length. Moreover, the SOVA model is under-resolved and thus not well fitted for validation of the models for tsunami propagation in large regions. To assess the performance of the Boussinesq-type models, we have therefore employed two models for full potential flow: namely, a 2-D traditional boundary integral model (Pedersen 2005) that is related to that of Dold (1992), and a new 3-D model that combines resolution in panels with Fourier transforms (Clamond et al. 2001; Fructus et al. 2005; Grue 2002).

APPENDIX 2: VELOCITY PROFILES AND UNIDIRECTIONAL WAVES

In shallow water theory there is no vertical variation of the horizontal velocity. Boussinesq theory, on the other hand, implies a parabolic velocity profile:

$$\vec{v} = \vec{v}_s + z\nabla\frac{\partial \eta}{\partial t} - \frac{1}{2}z^2\nabla\nabla\cdot\vec{v} \quad (6)$$

where $\vec{v}_s$ is the surface velocity and the $\vec{v}$ in the last term on the right-hand side may be replaced by the surface velocity without loss of accuracy. We need this profile for comparisons and exchange of data with the more general models.

The various models utilize different primary unknowns. In particular, the Boussinesq models are expressed in terms of surface elevations and depth-averaged velocities/potentials. The full potential flow methods involve surface elevation and velocities/potentials at the surface, whereas the SOVA model discretizes the whole velocity field and employs volume fractions and localizes the surface at grid cells that are partially filled with water. Moreover, the different theories imply different relations between surfaces and velocities for propagating waves. The compatibility problem is further accentuated by the fact that the SOVA model must be run with rather coarse resolution, making accurate extraction of surface velocities and elevations difficult. When the generation and early propagation have been computed by the radial SOVA model, surface and depth-averaged velocity are extracted and conveyed to the Boussinesq model. However, the surface is not accurately presented in the impact model due to coarse resolution. Moreover, the impact model and the long wave propagation model yield different dispersion properties. Hence, a direct adoption of both surface elevation and averaged velocity from the impact model will cause noise and artificial reflection in the propagation model. Alternatively, only the surface elevation is extracted and the velocity is computed from the assumption of radially diverging waves. For large r (far from impact center) we then have:

$$\sqrt{\frac{h}{g}}\left(\bar{u} - \frac{h^2}{6}\frac{\partial^2 \bar{u}}{\partial r^2}\right) = \eta - \frac{1}{4h}\eta^2 - \frac{1}{2}\int_{\infty}^{r}\frac{\eta}{r}dr \equiv R \quad (7)$$

where $\bar{u}$ is the vertically averaged horizontal velocity component. This relation is derived below. We observe that the right-hand side is singular for $r = 0$. It is essential that Equation 7 is written in an implicit manner, with the double derivative expressed in $\bar{u}$ instead of η. Otherwise, short-scale noise would be severely augmented. From Equation 6 we may then obtain the following relations between the surface, bottom, and depth-averaged velocities:

$$u_s = 2R - \bar{u}\,,\; u_b = \frac{3}{2}\bar{u} - \frac{1}{2}u_s \quad (8)$$

where u_s and u_b are the surface and bottom velocity, respectively, and R is as defined in Equation 7. The first relation may be used to convey fields from the Boussinesq solution to full potential theory. When combined with Equation 7 it also provides a route from the SOVA model to the full potential theory models.

To derive Equation 7 we first we note that constant depth implies that the depth-averaged velocity and the potential are related through $\bar{u} = \partial\phi/\partial r$. Differentiation of Equation 4 with respect to r then yields Boussinesq equations on the form

$$\frac{\partial \bar{u}}{\partial t} + \bar{u}\frac{\partial \bar{u}}{\partial r} + g\frac{\partial \eta}{\partial r} - \frac{h^2}{3}\frac{\partial}{\partial r}\left[\frac{1}{r}\frac{\partial}{\partial r}\left(r\frac{\partial \bar{u}}{\partial t}\right)\right] = 0 \quad (9)$$

$$\frac{\partial \eta}{\partial t} = -\frac{1}{r}\frac{\partial}{\partial r}[r(h+\eta)\bar{u}] \quad (10)$$

If we expand the spatial derivatives in these equations we obtain terms containing factors r^0, $1/r$, and $1/r^2$. When the terms with reciprocal powers of r are deleted in Equations 9 and 10 we retrieve the equations for plane waves. For large r,

and thus small curvatures of the wave-crests, these terms will be small. Moreover, if we enter a "moving" coordinate system $\xi \equiv x - c_0 t, t$ with $c_0 = \sqrt{gh}$ waves will undergo only slow temporal changes in the new coordinates, meaning that time derivatives are small. Observing that also nonlinear and dispersive terms are small we may transform Equations 9 and 10 to:

$$h\frac{\partial \bar{u}}{\partial \xi} - c_0\frac{\partial \eta}{\partial \xi} = -\frac{h\bar{u}}{\xi + c_0 t} - \frac{\partial}{\partial \xi}(\bar{u}\eta) - \frac{\partial \eta}{\partial t} + \text{h.o.} \tag{11}$$

$$c_0\frac{\partial \bar{u}}{\partial \xi} - g\frac{\partial \eta}{\partial \xi} = \bar{u}\frac{\partial \bar{u}}{\partial \xi} + \frac{h^2}{3}\frac{\partial^3 \bar{u}}{\partial \xi^3} + \text{h.o.} \tag{12}$$

where the leading terms are collected on the left-hand sides and "h.o." indicates negligible contributions from combination of nonlinearities or dispersion terms with reciprocals of r. We observe that the left-hand sides differ by a constant factor, only, and that we through shallow water theory have:

$$\bar{u} = c_0 \eta / h \tag{13}$$

provided there is quiescent water for some large r. This relation may then be employed to eliminate $\bar{u}$ from all terms on the right-hand sides of Equations 11 and 12, save the dispersion term. Next, we may combine the equations to eliminate $\partial\eta/\partial t$ and achieve an expression for $\bar{u}$ in terms of η:

$$\sqrt{\frac{h}{g}}\left(\frac{\partial \bar{u}}{\partial \xi} - \frac{h^2}{6}\frac{\partial^3 \bar{u}}{\partial \xi^3}\right) = \frac{\partial \eta}{\partial \xi} - \frac{1}{4h}\frac{\partial}{\partial \xi}(\eta^2) - \frac{1}{2}\frac{\eta}{\xi + c_0 t} \tag{14}$$

Re-insertion of r as spatial variable and integration then yields Equation 7. Naturally, we could also have replaced $\bar{u}$ in the triple-derivative term by η, but the resulting equation would then be less useful, even if explicit.

APPENDIX 3: SOLITARY WAVES AND OPTICS

The solitary wave is a single-crested wave of permanent shape and constant celerity that may exist due to the combined action of nonlinearity and dispersion. The concept of solitary waves goes back to the first half of the nineteenth century (Russell 1845), and has retained interest in the context of surface gravity waves since. From the end of the sixties throughout the seventies, the solitary wave was fashionable in various physical settings and a number of its remarkable properties, manifested through closed-form mathematical solutions, came to light. These include the particle-like interaction properties for small, but finite, amplitudes, and the genesis of solitary waves from general initial conditions. Most of the explicit results are confined to dispersive long wave theory, in particular the KdV equation, but numerical and perturbation solutions do exist for solitary waves within full potential theory as well. While the KdV and the Boussinesq equations yield solitary wave solutions of arbitrary amplitude, the full theory predicts a maximum height $A = 0.83h$, while amplitudes exceeding $0.78h$ and $0.72h$ yield instability in 2-D and 3-D, respectively (Kataoka et al. 2004; Tanaka 1986). A number of properties of solitary waves are described in the review (Miles 1980).

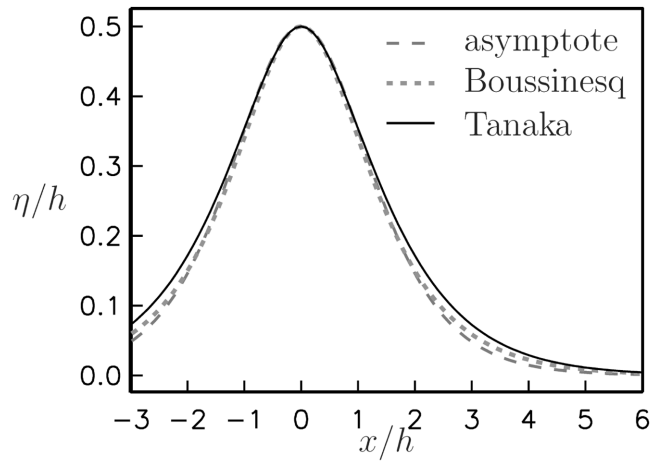

Fig. 19. Surface profiles for a solitary wave of height $A = 0.5h$ according to different approximations as explained in the text.

The surface elevation of a gravity solitary wave reads:

$$\frac{\eta}{h} = Y\left(\frac{A}{h}, \frac{x - ct}{h}\right)$$

$$= \frac{A}{h}\cosh^{-2}\left[\sqrt{\frac{3A}{4h}}\left(\frac{x - ct}{h}\right)\right]\left[1 + O\left(\frac{A}{h}\right)\right] \tag{15}$$

where c is the celerity (see below), Y a form function, and the rightmost expression is the asymptotic ($A/h \to 0$) solution consistent with the KdV equation. It is noteworthy that while the solitary wave in principle has infinite extension, though with exponentially decay on the outskirts, it displays a length scale that is in inverse proportion to the square root of A. For larger amplitudes the solutions for the KdV equations, the Boussinesq equations and full potential theory differ. An example, $A/h = 0.5$, is depicted in Fig. 19. Even for this quite high amplitude, there are only moderate differences between the Boussinesq solution and full potential theory.

The basis of the optics for solitary waves is the dependence of the energy density per crest length E, and the wave celerity c upon the equilibrium depth h and amplitude A

$$E(A, h) = \varepsilon\left(\frac{A}{h}\right)\rho g h^3 = \frac{8\rho g}{3^{\frac{3}{2}}}\left(\frac{A}{h}\right)^{\frac{3}{2}}\left[1 + O\left(\frac{A}{h}\right)\right]\rho g h^3$$

$$c(A, h) = C\left(\frac{A}{h}\right)(gh)^{\frac{1}{2}} = \left[1 + \frac{A}{2h} + O\left(\frac{A}{h}\right)^2\right](gh)^{\frac{1}{2}} \tag{16}$$

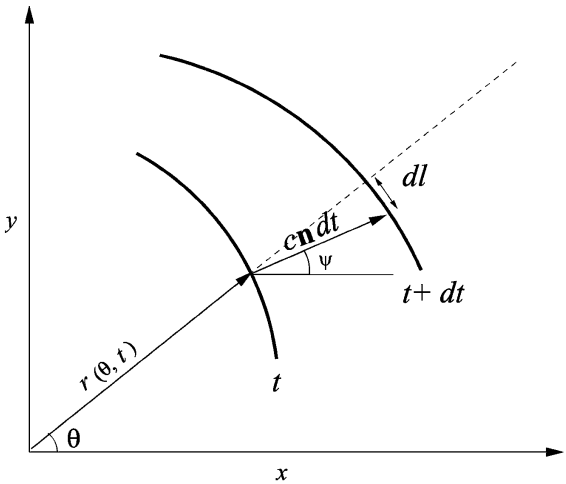

Fig. 20. Geometry and definitions for the optics. The wave crest is plotted at times t and $t + dt$.

The rightmost expressions are asymptotic approximations for A/h <<1. From Tanaka's method (Tanaka 1986) we may tabulate the functions ε and C for general A/h. Inserting the solitary wave solutions of the Boussinesq equations into the appropriate energy expressions we may also tabulate approximate functions ε and C that presumably are more consistent with our form of the Boussinesq Equations 1 and 2. However, it should be noted that the Boussinesq equations on this form are not exactly energy conserving. The different options for the energy density and wave celerity are displayed in Fig. 11.

In analogy to optics for sinusoidal waves, the basic assumption is that the relations (Equation 16) are valid also for gently curved and modulated solitary wave crests in slowly varying depths. Introducing some suitable parameterization for a wave crest we may then establish equations for its evolution. A crest will advance in time with the rate c in the direction perpendicular to itself, and we recognize rays as trajectories that are normal to the crest at all times. The energy density E times the arc length of the crest between two close rays, meaning the total energy between the rays, is assumed to remain constant. This leads to a coupled nonlinear set of equations for the amplitude distribution and the ray/crest deformations (Miles 1977; Reutov 1976; Pedersen 1994). In the present context it is convenient to parameterize the crest in polar coordinates, which means that the position of the crest is given by $r = r(\theta,t)$ (see Fig. 20). We note that this is different from the common use of optics for sinusoidal waves where fans of rays are parameterized as time trajectories and computed first, followed by the application of a transport equation for the amplitude.

The flux through the chord θ = const. is given by:

$$F = E\frac{dl}{dt} = -E\tan(\psi - \theta) = -E\frac{r_\theta}{r}c \tag{17}$$

Energy conservation then yields:

$$\frac{\partial}{\partial t}(E\sigma) = -\frac{\partial F}{\partial \theta} \tag{18}$$

where $\sigma = \sqrt{r^2 + r_\theta^2}$ is the arc length per θ. For the celerity we obtain:

$$\frac{\partial r}{\partial t} = \frac{c}{\cos(\theta - \psi)} = \frac{\sigma c}{r} \tag{19}$$

We observe that Equations 18 and 19 constitute a coupled set of equations for amplitude A and position r which must be solved simultaneously. Both equations are discretized in space by finite differences and an iterative time integration that mimics the Crank-Nicholson method. For cases with either plane wave motion or radial symmetry, these equations simplify to:

$$E(A, h)\xi^p = \text{const.}, \frac{d\xi}{dt} = \pm c(A, h) \tag{20}$$

where ξ is the spatial coordinate, x or r, and p equals unity for radial symmetry and zero for a plane wave, respectively. Employing the approximate expressions in Equation 16 we find:

$$A = A_0\frac{h_0}{h}\left(\frac{r_0}{r}\right)^{\frac{2}{3}p} \tag{21}$$

where A_0, h_0, and r_0 define a reference state. This equation is the basis of the discussion of far-field behavior of solitary waves given in the "Optical Approximation and Asymptotic Behavior in the Far-Field" section. By formal perturbation expansions, higher order optics may be developed, as in Ko et al. (1978) for the radially symmetric case and in Pedersen (1994, 1996) for general crest shapes and variable depth. Several new features are then included. Relevant in the present context are the shape modifications and diffraction, in the sense that the leading crest leaks and a trailing long elevation or trough is formed. In the symmetric case the height of the diffracted wave becomes:

$$A_D = 2\frac{3^{\frac{1}{2}}h^{\frac{3}{2}}}{A^{\frac{1}{2}}}\left(\frac{dh}{d\xi} + p\frac{2h}{9\xi}\right) \tag{22}$$

where ξ has the same meaning as in Equation 20. The shape modifications are of the same magnitude as the quantity A_D. Herein we are not primarily interested in these higher order modifications as such, but rather employ the relation:

$$F \equiv A_D/A \ll 1 \tag{23}$$

as an a priori validity criterion for the optics. Generally it turns out that the application of optics is more restricted for solitary waves than for sinusoidal waves (see also discussion in Miles

1980). For constant depth Equations 21–23 imply that F is independent of r. This means that the increased wavelength linked to the attenuation due to radial spreading is counterbalanced by the decrease in curvature of the wave front as far as validity of the optics is concerned. For a given bottom gradient we observe that F decreases with increasing amplitude. This is simply due to the inverse relation between height and length of solitary waves, which imply that the requirement of mild bathymetric variation is relaxed for the higher amplitudes. However, for the higher amplitudes we should employ tabulated $\varepsilon(A/h)$ and $C(A/h)$ from the Tanaka's solution rather than asymptotic formulas for small A/h. In shoaling water the waves may eventually reach the maximum amplitude, $A/h = 0.72$ and break. Kulikovskii and Reutov (1976) attempted to include breaking in an optical description, assuming that the crest during shoaling remained at the critical amplitude as a spilling breaker. However, there is no firm support for this assumption and in most applications the transformation to a traditional breaking bore of asymmetric shape seems more likely. Hence, the optical description should be abandoned as soon as breaking do occur.

The verification and application of the ray theory are presented in the "Qualitative Features—Simplified Computations" section.